

Scattering Observables from One- and Two-Body Densities: Formalism and Application to $\gamma^3\text{He}$ Scattering

Harald W. Griesshammer^{abc1}, Judith A. McGovern^{d2},
Andreas Nogga^{e3} and Daniel R. Phillips^{fgh4}

^a *Institute for Nuclear Studies, Department of Physics,
The George Washington University, Washington DC 20052, USA*

^b *Department of Physics, Duke University, Box 90305, Durham NC 27708, USA*

^c *High Intensity Gamma-Ray Source, Triangle Universities Nuclear Laboratories,
Box 90308, Durham NC 27708, USA*

^d *School of Physics and Astronomy, The University of Manchester,
Manchester M13 9PL, UK*

^e *IAS-4, IKP-3 and JCHP, Forschungszentrum Jülich, D-52428 Jülich, Germany*

^f *Department of Physics and Astronomy and Institute of Nuclear and Particle Physics,
Ohio University, Athens OH 45701, USA*

^g *Institut für Kernphysik, Technische Universität Darmstadt, 64289 Darmstadt, Germany*

^h *ExtreMe Matter Institute EMMI, GSI Helmholtzzentrum für Schwerionenforschung
GmbH, 64291 Darmstadt, Germany*

Abstract

We introduce the transition-density formalism, an efficient and general method for calculating the interaction of external probes with light nuclei. One- and two-body transition densities that encode the nuclear structure of the target are evaluated once and stored. They are then convoluted with an interaction kernel to produce amplitudes, and hence observables. By choosing different kernels, the same densities can be used for any reaction in which a probe interacts perturbatively with the target. The method therefore exploits the factorisation between nuclear structure and interaction kernel that occurs in such processes. We study in detail the convergence in

¹Email: hgrie@gwu.edu; permanent address: *a*

²Email: judith.mcgovern@manchester.ac.uk

³Email: a.nogga@fz-juelich.de

⁴Email: phillid1@ohio.edu

the number of partial waves for matrix elements relevant in elastic Compton scattering on ^3He . The results are fully consistent with our previous calculations in Chiral Effective Field Theory. But the new approach is markedly more computationally efficient, which facilitates the inclusion of more partial-wave channels in the calculation. We also discuss the usefulness of the transition-density method for other nuclei and reactions. Calculations of elastic Compton scattering on heavier targets like ^4He are straightforward extensions of this study, since the same interaction kernels are used. And the generality of the formalism means that our ^3He densities can be used to evaluate any ^3He elastic-scattering observable with contributions from one- and two-body operators. They are available at <https://datapub.fz-juelich.de/anogga>.

Suggested Keywords: Effective Field Theory, Compton scattering, ab initio calculations, three-body system, few-body system, electromagnetic reactions, reactions with external probes

1 Introduction

The structure of nuclei is usually investigated by some probe, *e.g.* by a process where an external particle interacts rather weakly with the nucleons of the nuclear target. One can then separate the dynamics of the strong interactions that bind the nucleus from the interaction of the nucleons with the probe and, to a high degree of accuracy, evaluate cross sections using expectation values of well-defined operators with respect to a nuclear wave function. For light nuclei, this has been extensively pursued for example in electron scattering [1–5], Compton scattering [6], weak decays and interactions of neutrinos with nuclei [7–10] and also to investigate Physics beyond the Standard Model [11, 12].

Theoretical descriptions of this problem require two ingredients: first, a reliable “interaction kernel”, *i.e.* the one- and few-body currents to which the external probes couple (“reaction mechanism”); and second, accurate eigenstates of the Hamiltonian for the nucleus (“structure”). We emphasise that this separation of the ingredients is only valid if both are evaluated consistently in the same framework. Here we employ Chiral Effective Field Theory (χ EFT)—see *e.g.* refs. [13–16] for recent reviews—as such a framework.

In this presentation, we show that matrix elements of two-body currents can be re-expressed as the trace of appropriately defined two-body densities with two-body-current matrix elements. Similarly, the one-body pieces of the matrix element are expressed as convolutions of one-body densities with the relevant one-body operator matrix elements. Technically, what we construct should be called “transition density amplitudes” because they describe a quantum mechanical matrix element in which the quantum numbers and momenta of the nucleon or nucleon pair are not necessarily the same before and after the collision. In a slight abuse of language we will, for brevity’s sake, refer to them as “transition densities” or “densities”. These densities can be directly generated from wave functions that are solutions of the non-relativistic Schrödinger equation for state-of-the-art two- and three-nucleon interactions. They are not dependent on the particular external probe, so the nuclear-structure piece of the calculation is factorised from the reaction mechanism.

It is hugely advantageous to strictly separate the two aspects: producing densities on the one hand, and convoluting them with interaction kernels on the other.

Such factorisation leads to marked gains in efficiency, since the one- and two-body densities can be computed once and stored. This most costly part of the evaluation can then be recycled to obtain results for a variety of reactions on the nucleus of interest: with such densities in hand, the evaluation of external-probe matrix elements requires only the convolution with appropriate interaction kernels that encode the one- and two-body current operators in the momentum-spin basis. The computational effort associated with this structure piece of the calculation increases significantly with A , but highly parallelised and optimised codes exist that solve for the wave functions of light nuclei. Constructing densities from those wave functions is straightforward.

In addition, densities can be provided in the machine-independently readable `hdf5` format, so that other groups can use the nuclear-structure part in a well-defined manner for their own evaluations. This separation is also much more reliable because interaction kernels can be prepared and benchmarked for several nuclei before applying them to previously-

unstudied systems, and because new densities can likewise be tested against known processes before applying them to new reactions. Computational resources and development can be focused on densities, which are then used in a variety of processes.

Indeed, separating the nuclear-structure information from the operators that describe the interaction with external probes is not without precedent. An analogous strategy has been used for many years in lattice QCD, where gauge configurations for a particular lattice and lattice action are computed and stored. The relatively cheap evaluation of quark correlators is then carried out separately—often for different external probes—without re-generating the gauge configurations. Likewise, transitions using shell-model wave functions use one-body density operators constructed from a sum of shell-model orbitals with occupancies obtained via the diagonalisation in the model space. Those density operators can then be contracted with a variety of operator matrix elements to yield observables; see for example ref. [17–19] for recent applications.

Here, we will go beyond simple densities and also allow for momentum transfer into the nuclear system. This extension is facilitated by the fact that our wave functions are obtained by solving momentum-space Faddeev equations. Thus, in contrast to the shell-model case, the densities we employ are defined in momentum space and are functions of the Jacobi momenta for the three-body system, of the corresponding Faddeev angular-momentum quantum numbers, and of momentum transfer and of energy.

We show how one- and two-body densities provide a common foundation for elastic reactions, and illustrate their use in elastic Compton scattering as an example of the general set-up. This process is especially well suited for our endeavour because a substantial fraction of its typical matrix element comes from “two-body currents”. The two-body densities are therefore key elements of our approach. Of course, amplitudes involving the trace of two-body densities play a small but important role in processes such as electron and dark-matter scattering too, but their contribution to Compton observables is more prominent.

In this first application, we restrict ourselves to ${}^3\text{He}$, whose one- and two-body densities are publicly available at <https://datapub.fz-juelich.de/anogga>. They are defined in momentum space, for a wide range of both cm energies and momentum-transfers, in terms of the Jacobi momenta for the three-body system and the corresponding Faddeev angular-momentum quantum numbers. At present, they are based on two combinations of local NN and 3N interactions which provide sufficiently different, realistic numerical challenges: AV18 with the Urbana-IX 3N interaction [20, 21] (AV18+UIX), which is relatively “hard” and a popular choice for testing new methods, or the considerably softer chiral Idaho N³LO interaction at cutoff 500 MeV [22] with the $\mathcal{O}(Q^3)$ χ EFT 3N interaction of variant “b” of ref. [23] (Idaho N³LO+3NFb).

We check the results obtained with these densities against matrix elements which were calculated independently using a different technique. This ensures the numerical correctness of our ingredients and allows us to quantify the efficiency and decrease in computational cost of the new method. Our focus is on Compton scattering off ${}^3\text{He}$, where previous work obtained nuclear matrix elements by integrating the interaction kernel directly with the wave function of the nucleus. In the formulation of refs. [24–28], which we now call the “traditional approach”, the evaluation of two-body-current matrix elements for $A = 3$

carried significant numerical cost: dramatically more than for $A = 2$, since extra integrations over the momentum of a third nucleon were performed.

We also choose this process as a test since it has been the focus of several dedicated experiments in the last decade. The High-Intensity Gamma-ray Source (HI γ S) at the Triangle Universities Nuclear Laboratory (TUNL), the Mainz Microtron (MAMI), and MAX-IV at Lund have all investigated elastic Compton scattering from light nuclei including ${}^6\text{Li}$ [29], ${}^4\text{He}$ [30, 31], the deuteron [32, 33], and others [34]. Measurements on ${}^3\text{He}$ are imminent at HI γ S [35] and MAMI [36]. Much of the motivation for such data is to constrain the electromagnetic polarisabilities of the neutron [6, 37].

However, the computational cost of calculations in the “traditional” approach is prohibitive for all but the lightest targets on this list. The new densities-based approach opens the way for calculations of elastic Compton scattering on ${}^4\text{He}$ and beyond. Indeed, the extension from $A = 2$ and $A = 3$ to a wider range of nuclei is conceptually straightforward and does not involve additional major computational effort—beyond that already expended by nuclear-structure practitioners to obtain wave functions for the A -body ground state. The computational cost of one- and two-body densities for, say, the spin-zero nuclei ${}^4\text{He}$ and ${}^{12}\text{C}$ varies by orders of magnitude, but the Compton convolutions use the same interaction kernels and are of comparable computational complexity.

We emphasise that our goal here is not to provide new results for ${}^3\text{He}$ Compton scattering with a better description of the physics of the process. Rather, we aim to improve the computational efficiency. The new approach speeds up the evaluation of Compton matrix elements by a factor of 10 or more. This enables concomitant improvements in the numerical accuracy: we can now include many more channels in the computation of two-body-current matrix elements. The convergence studies presented in sect. 3.3 would come at very high computational cost in the “traditional” approach.

The new formulation can of course be extended in various directions. In processes or régimes where three- and higher-body contributions to the interaction kernel are needed, one can employ three-, four-body, \dots , densities, although the storage required does grow dramatically. One can also envision adding inelastic reactions and transmutations (Z altered by reaction), like electro-disintegration, β decay, inelastic neutrino scattering, inelastic Compton scattering, or photo-production of charged pions. In this paper, however, we restrict ourselves to elastic reactions; and hence, for Compton scattering, to energies below the pion-production threshold, which in practice means $\omega \lesssim 120$ MeV.

On the other hand, the present form of the framework provides an incomplete description at low energies, since it relies on a subset of $A - 2$ spectator nucleons not participating in the reaction. This is approximately true if the energy inserted by the external probe is large compared to the nuclear binding scale; see also sect. 2.1. The time-scale set by the interaction kernel is then much smaller than that of the interactions which lead to nuclear binding. To a good approximation, the probe then interacts with single nucleons or correlated nucleon pairs, and the nuclear response is not collective. In Compton scattering, this is no longer the case at lower energies [6, 38]; see also ref. [39]. There, “rescattering”, namely the interaction of all A nucleons with one another between photon absorption and emission, becomes an important reaction mechanism and should be added to the ones calculated

here. However, that is not the focus of this presentation. Rather we are concerned with the efficient calculation of the non-collective contributions which dominate above about 50 MeV, which is also where data is most likely to be taken to extract nucleon polarisabilities.

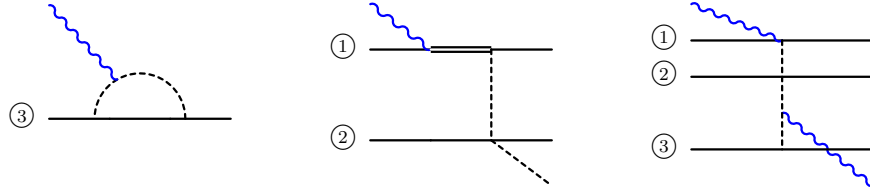
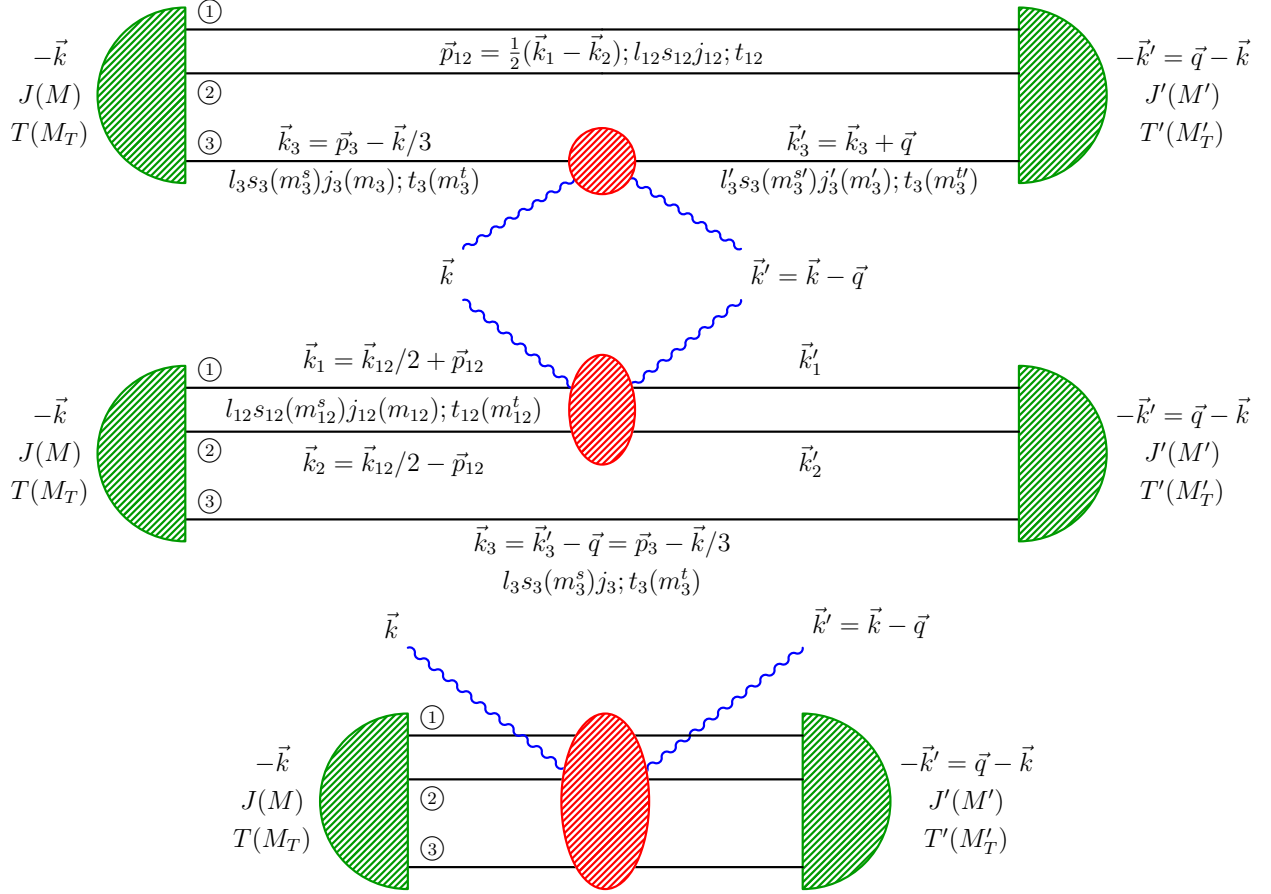
The presentation is organised as follows. Section 2 first provides an overview of the method, then explains how to construct the one- and two-body densities for a general elastic-scattering reaction on ${}^3\text{He}$, and closes with a discussion of the symmetries of those densities. Section 3 contains the premises and results of our analysis. In sect. 3.1, we define the interaction kernels. The one-body kernels are insertions of one-nucleon-spin operators with momentum transfer. The two-nucleon kernels are those of ${}^3\text{He}$ Compton scattering in the variant of Chiral Effective Field Theory (χEFT) with dynamical $\Delta(1232)$ degrees of freedom at next-to-next-to-leading order [N^2LO , $\mathcal{O}(e^2\delta^3)$] [38, 40]. We then discuss the amplitudes produced using one- and two-body amplitudes: choices of NN and 3N interactions (sect. 3.2), convergence with the number of partial waves and numerical stability (sect. 3.3), and finally comparison to the results of the previous, “traditional” approach (sect. 3.4). We provide the customary summary and outlook in sect. 4. Appendix A comments on an error in the original implementation of the one-body Compton-scattering kernel which does not affect the results for ${}^3\text{He}$ Compton scattering reported previously, within expected theory uncertainties. Appendix B concerns symmetries of matrix elements.

2 Defining Transition Densities

2.1 Overview

We first describe the concept, using our chosen example: Compton scattering. As mentioned in the Introduction, one important scale is set by the time between photon emission and photon absorption; according to the uncertainty principle, it is $\sim 1/\omega$. If this is much smaller than the time-scale on which nucleons interact (rescatter) inside the nucleus, then amplitudes can be expressed as an expectation value of operators acting on the nuclear bound state wave functions [24–27]. But what is more, because the nucleus is then “frozen in time”, the problem factorises into the Compton scattering reaction mechanism between the photon and the n *active nucleons* which directly interact with it, and a backdrop of $A - n$ *spectators* which do not¹. This allows us to separate the convolution into two parts: the reaction mechanism of the Compton event which is defined by the *interaction kernel* between the photon and n nucleons; and the *n-body density*. The latter is the probability amplitude for the combination of n active nucleons to change quantum numbers, and thus accounts for the presence of all $A - n$ spectators. Figure 1 illustrates the separation, with the interaction kernel depicted as a red ellipse. We will expand on this figure in the subsequent presentation. Figure 2 provides example contributions to one- and few-body interaction kernels of various reactions, *i.e.* to the red ellipses of fig. 1.

¹Note that for us, a “spectator” is every nucleon that is not involved in the interaction kernel. We do *not* use that term for the “outermost” nucleon in Jacobi coordinates. Indeed, we choose it to be the spectator to a two-body matrix element, but the active participant in the one-body matrix element; see below.



The *one-body density* ($n = 1$, illustrated for $A = 3$ in the top of fig. 1) is the transition amplitude to find one nucleon labelled “ A ” with specific spin projection m_A^s inside a nucleus with momentum $-\vec{k}$, to have it absorb a momentum transfer \vec{q} and re-arrange spin quantum numbers, and finally be reincorporated into the A -body system in such a way that the nucleus remains coherent and in its ground state.

Likewise, the *two-body density* ($n = 2$, centre of fig. 1 for $A = 3$) is the transition amplitude for a two-nucleon state with total momentum \vec{k}_{12} , intrinsic relative momentum of magnitude p_{12} and specific quantum numbers of the pair (relative to the $(A - 2)$ spectators) to absorb a momentum transfer \vec{q} and re-arrange its spin and angular-momentum quantum numbers, before finally being absorbed back into the nucleus.

Few-body densities for $n \geq 3$ active nucleons can also be defined as needed; see bottom of fig. 1 for $n = 3$. Aside from the rescattering contributions mentioned above, most important are however usually the one-body and two-body densities. It is a fundamental advantage of χ EFT that it provides a well-defined procedure to predict such a hierarchy of n -body mechanisms [41–44]; see also refs. [13–16].

We therefore carefully discuss the generation, numerical stability and convergence of the one- and two-body densities for the $A = 3$ system using ${}^3\text{He}$, opening the path towards other applications of these, and of densities for heavier nuclei like ${}^4\text{He}$.

2.2 Kinematics and Partial-Wave Decomposition

Consider a nucleus of A nucleons which in the initial state has total angular momentum J , spin-projection M onto the z -axis, and isospin-projection M_T (*i.e.* definite charge). Several isospins T may contribute. In the ${}^3\text{He}$ nucleus, for example, only states with total angular momentum $J = \frac{1}{2}$ and total isospin projection $M_T = \frac{1}{2}$ contribute; the dominant contribution is from the iso-doublet $T = \frac{1}{2}$, but isospin breaking induces small $T = \frac{3}{2}$ components into the ${}^3\text{He}$ wave functions. A sophisticated description of nuclear processes needs to take these into account, and ours does.

Concerning kinematics, the motion of the incident probe (the photon, in our example) defines the z -axis, $\vec{k} = |\vec{k}| \vec{e}_z$, which is also the quantisation axis for spin-projections. Scattering takes place in the xz -plane, and the momentum transfer into the nucleus is \vec{q} . We will use the centre-of-mass (cm) frame of the probe-target system, *i.e.* the momentum of the incident nucleus is $-\vec{k}$. With our choice of conventions, three variables suffice to characterise the process completely: the magnitude of \vec{k} (since its direction is fixed along the z -axis), the magnitude of \vec{q} , and the angle between the two (since both span the scattering plane). In our primary example, elastic Compton scattering, the outgoing photon momentum is $\vec{k}' = \vec{k} - \vec{q}$ and $|\vec{k}'| = |\vec{k}|$, so that only two variables are independent; see sect. 3.1.1. For electromagnetic form factors, one sets in addition $\vec{k} = \vec{q}$ as the momentum of the virtual photon in the $A\gamma^*$ cm frame, so that there is only one independent variable left. The densities we produced thus far are characterised by two independent variables only, but the formalism we discuss now is more general.

For $A \geq 4$, several kinds of Jacobi momentum coordinates can be defined which do not just differ by a permutation of the nucleons. Few-body wave functions are however usually

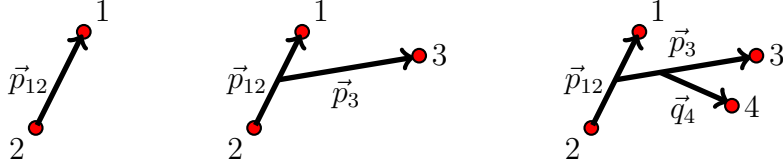


Figure 3: Jacobi coordinates of the two-, three- and four-nucleon systems, and the assignments of relative momenta \vec{p} , \vec{q} between constituents.

most efficiently represented in a hierarchical framework like the one shown in Figure 3.

Independently of the size of the nuclear systems, we always choose a definition that singles out the (12) subsystem for the application of two-body operators, and the last (A th) nucleon for one-body operators, *e.g.* the third one for $A = 3$, or fourth for $A = 4$. As is traditional for Jacobi coordinates, we call the (12) system the “innermost” pair and the A th nucleon the “outermost” nucleon. This terminology of course does not mean that these nucleons are spatially nearest to or farthest from the centre of the nucleus.

We now describe in detail those kinematics and quantum numbers which are relevant for the factorised computation. We label the momenta of the individual nucleons in the cm frame as $\vec{k}_1, \vec{k}_2, \vec{k}_3, \dots$. The total momentum is of course conserved and zero, $\vec{k} + \sum_i^A \vec{k}_i = 0$. For $A = 3$, fig. 1 summarises the pertinent variables for computations involving one-body (top) and two-body (centre) densities, as well as for three-body densities (bottom), which are however not required for our present purposes.

For the one-body densities, assuming that all nucleons have equal mass, the relative momentum of the “outermost”, active, nucleon with respect to all others is defined by

$$\vec{p}_A = \frac{A-1}{A} \vec{k}_A - \frac{1}{A} \sum_{i=1}^{A-1} \vec{k}_i, \quad (2.1)$$

see top of fig. 1. The relative and total pair momenta of the “innermost” pair are

$$\vec{p}_{12} = \frac{1}{2} (\vec{k}_1 - \vec{k}_2), \quad \vec{k}_{12} = \vec{k}_1 + \vec{k}_2. \quad (2.2)$$

It is this “innermost” pair which we define as the “active pair” for two-body densities, *i.e.* the one which interacts with the external probe; see second row of fig. 1. In the $A = 3$ system, which is our primary focus, the relative momentum of the third nucleon with respect to the inner pair is

$$\vec{p}_3 = \frac{2}{3} \vec{k}_3 - \frac{1}{3} (\vec{k}_1 + \vec{k}_2) = \vec{k}_3 + \frac{1}{3} \vec{k}, \quad (2.3)$$

which will allow us to later trade dependence on the momentum \vec{k}_3 of an individual nucleon for dependence on the total momentum \vec{k} of the nucleus.

We denote the ^3He state of spin-projection M by $|M\rangle$, suppressing labels for the other quantum numbers JM_T and bound-state energy. This is an eigenstate of the Hamiltonian of the nucleus at rest, and an eigenstate of both the total angular-momentum operator and

its z -component. We project this state onto a partial-wave-decomposed eigenstate of the Jacobi momenta and spins (cf. below), defining a momentum-space wave function

$$\psi_\alpha(p_{12}p_3) = \langle p_{12}p_3\alpha|M \rangle . \quad (2.4)$$

This basis is parametrised by the magnitudes of the relative pair-momentum p_{12} and the relative momentum p_3 of the third nucleon with respect to the pair. We denote the orbital angular momentum, spin, and isospin quantum numbers of our Jacobi-momentum basis using the collective label α . The orbital angular momentum l_{12} and the spin s_{12} of the (12) subsystem combine to give j_{12} . Similarly, l_3 and $s_3 \equiv \frac{1}{2}$ combine to give j_3 . Finally, j_{12} and j_3 are combined into the total angular-momentum magnitude J and z -projection M of the nucleus. The isospin t_{12} of the (12) subsystem and $t_3 \equiv \frac{1}{2}$ of the third particle are coupled to total isospin T . Therefore, the quantum numbers summarised in α are

$$|\alpha\rangle = |[(l_{12}s_{12})j_{12}(l_3s_3)j_3] JM, (t_{12}t_3)TM_T\rangle . \quad (2.5)$$

The Pauli principle guarantees that only states with $l_{12} + s_{12} + t_{12}$ odd enter in α . As both t_{12} and s_{12} can only have values of 0 or 1, the isospin of the (12) pair is actually set by

$$t_{12} = \frac{1}{2} [1 + (-1)^{l_{12}+s_{12}}] . \quad (2.6)$$

Since we compute $|M\rangle$ using isospin-violating NN and 3N interactions, the ket is *not* an eigenstate of the total isospin operator and has overlap with α s of both $T = \frac{1}{2}$ and $T = \frac{3}{2}$. On the other hand, we consider ${}^3\text{He}$ states with a specific spin-projection, so only α s with $J = \frac{1}{2}$ and the appropriate M have a non-zero overlap in eq. (2.4).

Primed variables denote quantum numbers of the final state $\langle M'|$. Thus, for example, \vec{k}'_3 is the momentum of particle 3 when it flows into the final state, and

$$\langle\alpha'|\equiv\langle[(l'_{12}s'_{12})j'_{12}(l'_3s'_3\equiv s_3)j'_3] J' M', (t'_{12}t'_3\equiv t_3) T' M'_T| . \quad (2.7)$$

Although we are mainly interested in $J = \frac{1}{2}$ and $M_T = \frac{1}{2}$ (the case of ${}^3\text{He}$) we leave both arbitrary, so we can display how the formulae would look for an arbitrary nucleus.

In this presentation, we restrict ourselves to elastic processes, *i.e.* the total angular momentum $J' = J$ and isospin projection $M'_T = M_T$ are conserved. This implies that the probe changes neither the charge of the struck nucleons, nor that of the spectators. Therefore, the third component of isospin is conserved for all particles, $m_i^{t'} = m_i^t$ with $i = 1, \dots, A$, and for all sub-systems, *e.g.* $m_{12}^{t'} = m_{12}^t$. However, interaction with the probe can change isospin and the wave function of the nucleus contains components with more than one T , so $T' \neq T$ is allowed in the densities. Whereas fermions remain fermions ($t'_3 = t_3 = \frac{1}{2}$), the isospin t_{12} of a fermion-pair can be changed by interaction with the probe. The extension to include transmutation and charge-transfer reactions ($J' \neq J$ and/or $M'_T \neq M_T$, *i.e.* $m_i^{t'} \neq m_i^t$ for some nucleon(s) i), like charged-pion photoproduction, β -decay or inelastic neutrino scattering, is straightforward and left to a future publication.

While J' is identical to its unprimed counterpart, we decide to keep its prime for out-states. Likewise, we keep the quantum numbers $s_3 = \frac{1}{2}$ and $t_3 = \frac{1}{2}$ explicit. Both choices

make it easier to track which spins and isospins are coupled. We do however replace $m_3^{t'}$ by m_3^t , and $m_{12}^{t'}$ by m_{12}^t .

Finally, we point out that the state $|M\rangle$ must be multiplied by an eigenstate of the nuclear cm momentum operator, to give the momentum of the incoming and outgoing states ($-\vec{k}$ and $-\vec{k}' = \vec{q} - \vec{k}$). Since in non-relativistic systems, this results only in an overall momentum-conserving $\delta^{(3)}(\vec{k} - \vec{k}' - \vec{q}) = \delta^{(3)}(\vec{k}'_1 + \vec{k}'_2 + \vec{k}'_3 - \vec{k}_1 - \vec{k}_2 - \vec{k}_3 - \vec{q})$, we do not include these momentum wave functions explicitly in what follows.

2.3 The One-Body Density

We first consider one-body densities. We define the nucleon which interacts with the probe to be the “outermost” one—the one with index 3 in the three-body system that we focus on; see fig. 1. Since we represent the nucleon as an iso-doublet consisting of the proton and neutron, the expectation values when the photon strikes the other two nucleons are identical and do not need to be calculated explicitly.

We start with a definition of the relevant operator and matrix element in a basis of single-nucleon momentum, spin, and isospin states:

$$\begin{aligned} & \langle \vec{k}'_3 | \langle s_3 m_3^{s'} | \langle t_3 m_3^{t'} | \hat{O}_3(\vec{k}, \vec{q}) | t_3 m_3^t \rangle | s_3 m_3^s \rangle | \vec{k}_3 \rangle \\ & \equiv \delta_{m_3^{t'} m_3^t} \delta^{(3)}(\vec{k}'_3 - \vec{k}_3 - \vec{q}) O_3(m_3^{s'} m_3^s m_3^t; \vec{k}_3; \vec{k}, \vec{q}) \quad , \end{aligned} \quad (2.8)$$

where \vec{k}_3 and \vec{k}'_3 are the third nucleon’s incoming and outgoing momenta. Here, the probe does not change the charge of the struck nucleon, $m_3^{t'} = m_3^t$. The nucleon-spin components are not necessarily conserved for spin-dependent interactions.

In this form, the probe’s cm momentum \vec{k} and the momentum-transfer \vec{q} are external parameters. Momentum conservation separates off the δ -distribution in $\vec{k}'_3 - \vec{k}_3 - \vec{q}$. For many applications, the operators do not explicitly depend on \vec{k}_3 , so that the frame used for the calculation does not matter as we will see below. But one complication that arises in Compton scattering in χ EFT at NLO and beyond is that O_A explicitly depends on the single-nucleon momentum \vec{k}_A . In a few- or many-body system, this will lead to a dependence on the relative momentum \vec{p}_A with respect to non-participating nucleons. Such effects depend on the nucleus and appear whenever boost corrections from the cm frame of the nucleus to the frame of the active (struck) nucleon must be considered. Therefore, we multipole-expand the \vec{k}_3 -dependence of the spin-isospin matrix elements in spherical coordinates up to multipolarity K_{\max} :

$$O_3(m_3^{s'} m_3^s m_3^t; \vec{k}_3; \vec{k}, \vec{q}) \equiv \sum_{K=0}^{K_{\max}} \sum_{\kappa=-K}^K \sqrt{\frac{4\pi}{2K+1}} (k_3)^K Y_{K\kappa}(\hat{k}_3) \tilde{O}_3(m_3^{s'} m_3^s m_3^t; K\kappa; \vec{k}, \vec{q}) \quad , \quad (2.9)$$

where \hat{k} is the unit vector (angular dependence) of \vec{k} . The prefactors guarantee that \tilde{O}_3 and O_3 are identical for \vec{k}_3 -independent operators or for $K = 0$. In Compton scattering, up to the order to which we work in χ EFT, it suffices to consider at most a linear dependence of

the operator on the nucleon momentum. Thus we have, so far, only calculated one-body densities up to $K_{\max} = 1$.

Let us, for concreteness, continue with ${}^3\text{He}$. Then, the matrix element of \hat{O}_3 is written as

$$\begin{aligned} \langle M' | \hat{O}_3(\vec{k}, \vec{q}) | M \rangle &= \sum_{\alpha\alpha'} \int dp_{12} p_{12}^2 dp_3 p_3^2 dp'_{12} p_{12}'^2 dp'_3 p_3'^2 \psi_{\alpha'}^\dagger(p'_{12}p'_3) \psi_\alpha(p_{12}p_3) \\ &\times \langle p'_{12}p'_3 [(l'_{12}s'_{12})j'_{12}(l'_3s_3)j'_3] J'M'(t'_{12}t_3)T'M_T | \hat{O}_3(\vec{k}, \vec{q}) \\ &\quad | p_{12}p_3 [(l_{12}s_{12})j_{12}(l_3s_3)j_3] JM(t_{12}t_3)TM_T \rangle . \end{aligned} \quad (2.10)$$

Now, the matrix elements $\langle \alpha' | \hat{O}_3 | \alpha \rangle$ enter, as well as the partial-wave momentum-space wave function $\psi_\alpha(p_{12}p_3)$ of ${}^3\text{He}$. Using Clebsch-Gordan coefficients $\langle j_1j_2m_1m_2 | jm \rangle$ in the convention of refs. [45, 46], we can explicitly decompose α so as to separate the spin-isospin quantum numbers of the pair from those of the third nucleon:

$$\begin{aligned} \langle M' | \hat{O}_3(\vec{k}, \vec{q}) | M \rangle &= \\ &\sum_{\alpha} \int dp_{12} p_{12}^2 \int dp_3 p_3^2 \sum_{\alpha'} \int dp'_{12} p_{12}'^2 \int dp'_3 p_3'^2 \psi_{\alpha'}^\dagger(p'_{12}p'_3) \psi_\alpha(p_{12}p_3) \\ &\times \sum_{m_3m_3^t} \langle j_{12}j_3(M - m_3)m_3 | JM \rangle \langle t_{12}t_3(M_T - m_3^t)m_3^t | TM_T \rangle \\ &\times \sum_{m'_3} \langle j'_{12}j'_3(M' - m'_3)m'_3 | J'M' \rangle \langle t'_{12}t_3(M_T - m_3^t)m_3^t | T'M_T \rangle \\ &\times \langle p'_{12}(l'_{12}s'_{12})j'_{12}(M' - m'_3), t'_{12}(M_T - m_3^t) | p_{12}(l_{12}s_{12})j_{12}(M - m_3), t_{12}(M_T - m_3^t) \rangle \\ &\times \langle p'_3(l'_3s_3)j'_3m'_3, t_3m_3^t | \hat{O}_3(\vec{k}, \vec{q}) | p_3(l_3s_3)j_3m_3, t_3m_3^t \rangle . \end{aligned} \quad (2.11)$$

Here and from now on, we directly impose the identities for spin-projections, $M = m_3 + m_{12}$, $M_T = m_3^t + m_{12}^t$ etc. The part relating to the (12) subsystem of spectators just gives the usual δ -distributions and a set of Kronecker- δ s in the quantum numbers of that subsystem. The matrix element on the last line of eq. (2.11) also contains a momentum-conserving δ -distribution—see eq. (2.8). We determine it using (2.3) and a corresponding relation for the primed momenta. This can be used to eliminate explicit dependence on \vec{k}_3 in favour of dependence on the cm momentum \vec{k} of the nucleus. The momentum-conserving δ -distribution of the operator is then

$$\delta^{(3)}(\vec{k}'_3 - \vec{k}_3 - \vec{q}) = \delta^{(3)}(\vec{p}'_3 - \vec{p}_3 - \frac{2}{3}\vec{q}) . \quad (2.12)$$

For the explicit evaluation of the matrix element and this δ -distribution, we insert the solid angle \hat{p}_3 of the third particle's momentum over which we need to integrate and introduce the three-momentum $\vec{p}_3 = p_3 \hat{p}_3$. The spherical harmonics then depend on the angles of $\widehat{\vec{p}_3 + \frac{2}{3}\vec{q}}$ and $\widehat{\vec{p}_3 - \frac{1}{3}\vec{k}}$ associated with linear combinations of the three-vectors \vec{p}_3 , \vec{q} and \vec{k} .

The wave-function overlap also needs to be evaluated at a shifted momentum magnitude $|\vec{p}_3 + \frac{2}{3}\vec{q}|$.

Inserting eqs. (2.8) and (2.9) into (2.11) gives the complete expression for the matrix element and thus the starting point for computations in the “traditional” approach. What is novel now is the recognition that the sums over quantum numbers can be factorised. The full matrix element can thus be written as:

$$\langle M' | \hat{O}_3(\vec{k}, \vec{q}) | M \rangle = \sum_{K=0}^{K_{\max}} \sum_{\kappa=-K}^K \sum_{\substack{m_3^s m_3^t \\ m_3^t}} \tilde{O}_3(m_3^s m_3^s, m_3^t; K \kappa; \vec{k}, \vec{q}) \rho_{m_3^s m_3^s}^{K \kappa; m_3^t M_T, M' M}(\vec{k}, \vec{q}), \quad (2.13)$$

where we define the one-body (transition) density by summing over those quantum numbers that are not involved in the interaction:

$$\begin{aligned} \rho_{m_3^s m_3^s}^{K \kappa; m_3^t M_T, M' M}(\vec{k}, \vec{q}) &:= \sum_{\alpha} \int dp_{12} p_{12}^2 \int dp_3 p_3^2 \sum_{\alpha'} \delta_{j_{12} j'_{12}} \delta_{l_{12} l'_{12}} \delta_{s_{12} s'_{12}} \delta_{t_{12} t'_{12}} \delta_{M_T M'_T} \\ &\times \sum_{m_3} \langle j_{12} j'_{12} (M - m_3) (M' - M + m_3) | J' M' \rangle \langle t_{12} t_3 (M_T - m_3^t) m_3^t | T' M_T \rangle \\ &\times \langle j_{12} j_3 (M - m_3) m_3 | J M \rangle \langle t_{12} t_3 (M_T - m_3^t) m_3^t | T M_T \rangle \\ &\times \langle l'_3 s_3 (M' - M + m_3 - m_3^s) m_3^s | j'_3 (M' - M + m_3) \rangle \langle l_3 s_3 (m_3 - m_3^s) m_3^s | j_3 m_3 \rangle \\ &\times \int d\hat{p}_3 Y_{l'_3 (M' - M + m_3 - m_3^s)}^{\dagger}(\widehat{\vec{p}_3 + \frac{2}{3}\vec{q}}) Y_{l_3 (m_3 - m_3^s)}(\hat{p}_3) \\ &\times \sqrt{\frac{4\pi}{2K+1}} |\vec{p}_3 - \frac{1}{3}\vec{k}|^K Y_{K \kappa}(\widehat{\vec{p}_3 - \frac{1}{3}\vec{k}}) \psi_{\alpha'}^{\dagger}(p_{12} |\vec{p}_3 + \frac{2}{3}\vec{q}|) \psi_{\alpha}(p_{12} p_3) . \end{aligned} \quad (2.14)$$

We present an operator form of this one-body density in eq. (2.27).

This convolution of operator matrix elements with the one-body density in (2.13) does not involve a sum over all the quantum numbers $\{j_3 l_3 m_3^l m_3\}$ of the active nucleon, but only over m_3^s . For the frequently-met case of $K = 0$, the density also does not explicitly depend on the momentum $-\vec{k}$ of the nucleus. Thus it is independent of the frame chosen and depends only on the momentum transfer \vec{q} .

This density is independent of the operator O_3 and so allows the evaluation of pertinent expectation values for any amplitude given by such a one-body expectation value. The structure derived here thus applies not only to Compton scattering, but also to many other reactions involving external probes. Such a separation can of course be done for any nucleus A , and is certainly feasible today for ${}^4\text{He}$ and for p -shell nuclei in the No-Core Shell Model. Once a nuclear-structure calculation has been performed, the one-body transition densities $\rho_{m_3^s m_3^s}^{K \kappa; m_3^t M_T, M' M}(\vec{k}, \vec{q})$ can be calculated and results for processes involving external probes can be generalised to more complex nuclei, without changing the reaction-dependent matrix elements \tilde{O}_A . In this sense, the two parts factorise.

As an example of how to convolute one-body operators with one-body densities, we consider the one-body contribution to a nuclear form factor. The operator \hat{O}_3 must then count

the number of protons or neutrons seen at a particular momentum transfer \vec{q} , *i.e.* at resolution $1/|\vec{q}|$. By taking $\vec{q} \rightarrow 0$, such a calculation also permits us to define the normalisation of the one-body densities.

For this \hat{O}_3 , the matrix element \tilde{O}_3 in eq. (2.13) is

$$\tilde{N}_3(m_3^{s'} m_3^s, m_3^t; K\kappa; \vec{k}, \vec{q}) := 3 \delta_{K0} \delta_{\kappa 0} \delta_{m_3^{s'} m_3^s} \times \begin{cases} \delta_{m_3^t, \frac{1}{2}} & \text{for protons} \\ \delta_{m_3^t, -\frac{1}{2}} & \text{for neutrons} \end{cases} . \quad (2.15)$$

Here, the symmetry factor of 3 (counting the indistinguishable, “active” nucleons) must be replaced by A in arbitrary nuclei. The resultant matrix element is

$$3 \sum_{m_3^s} \rho_{m_3^s m_3^s}^{(K=0)(\kappa=0);(m_3^t=\pm\frac{1}{2})(M_T=\frac{1}{2}),M'M}(\vec{k}, \vec{q}) , \quad (2.16)$$

see also sect. 3.1.2 for the relation to inserting Pauli spin operators. Summing over the single-nucleon isospins m_3^t then counts the number A of nucleons. At zero momentum transfer, the matrix element should be 2 (for $m_3^t = \frac{1}{2}$) or 1 (for $m_3^t = -\frac{1}{2}$). It follows that the one-body density of ${}^3\text{He}$ must obey:

$$\begin{aligned} 2\delta_{M'M} &\stackrel{!}{=} 3 \sum_{m_3^s} \rho_{m_3^s m_3^s}^{(K=0)(\kappa=0);(m_3^t=+\frac{1}{2})(M_T=\frac{1}{2}),M'M}(\vec{k}, \vec{q}=0) , \\ \delta_{M'M} &\stackrel{!}{=} 3 \sum_{m_3^s} \rho_{m_3^s m_3^s}^{(K=0)(\kappa=0);(m_3^t=-\frac{1}{2})(M_T=\frac{1}{2}),M'M}(\vec{k}, \vec{q}=0) . \end{aligned} \quad (2.17)$$

One-body densities are therefore dimensionless.

Indeed, eq. (2.14) shows that this normalisation is actually imposed by normalising the ${}^3\text{He}$ wave function to unity. However, the wave function is normalised by inserting a complete set of Faddeev components $\psi_\alpha(p_{12}p_3)$ inside ${}^3\text{He}$. That partial-wave expansion in quantum numbers α usually converges quickly, but is of course truncated. Thus, the norm of the wave function is in practice not exactly 1, but approaches 1 from below, with the difference from 1 quantifying the contribution of the missing partial waves. Since densities are computed using a finite set of partial waves, eq. (2.17) therefore gives results which are slightly smaller than 2 or 1, respectively. This is actually a better normalisation choice when evaluating matrix elements of short- or pion-range operators since it provides a more accurate normalisation of lower partial waves. If one were to set the norm of the *truncated* wave function to unity, contributions from those partial waves that are included in the sum would be artificially enhanced, distorting the results. We will discuss the numerical deviation from the ideal normalisation in sect. 3.3.1.

Storing one-body densities is quite cheap. For each set of kinematics (\vec{q}) and for a general spin- J nucleus with isospin-projection M_T , there are $2J + 1$ total-spin projections M, M' for both the incident and outgoing nucleons, 2 spin-projections $m_3^s = \pm\frac{1}{2}$ for the active nucleon both before and after the interaction, 2 isospin-projections $m_3^t = m_3^{t'} = \pm\frac{1}{2}$, and up to $(K_{\max} + 1)^2$ entries when the kernel needs to be multipole-expanded up to K_{\max} powers of \vec{k} . Thus, not accounting for symmetries or trivial zeroes, each nucleus needs file space for at most $8(K_{\max} + 1)^2 (2J + 1)^2$ numbers per kinematic point. This is just 128 entries for ${}^3\text{He}$ Compton scattering with up-to-linear boost effects, or a few kilobytes.

2.4 The Two-Body Density

We now turn to contributions with $n = 2$ “active” nucleons. In our convention, these only involve quantum numbers and momenta of the two “innermost” nucleons, labelled 1 and 2; see the central diagram of fig. 1 for the relevant kinematics and quantum numbers. Since we treat the nucleons in the nucleus as identical, the other pairs contribute equally and do not need to be considered explicitly. In Compton scattering, this kernel parametrises the interaction of both photons with irreducible two-nucleon currents mediated by charged pions; see fig. 4.

The matrix elements of the two-nucleon operators have the form

$$\begin{aligned} & \langle \vec{p}'_{12} \vec{k}'_{12} | \langle s'_{12} m'_{12} | \langle t'_{12} m'_{12} | \hat{O}_{12}(\vec{k}, \vec{q}) | t_{12} m_{12} \rangle | s_{12} m_{12} \rangle | \vec{p}_{12} \vec{k}_{12} \rangle \\ & = \delta^{(3)}(\vec{k}'_{12} - \vec{k}_{12} - \vec{q}) O_{12}(s'_{12} t'_{12} m'_{12} s_{12} t_{12} m_{12} m_{12}^s m_{12}^t; \vec{p}'_{12}, \vec{p}_{12}; \vec{k}, \vec{q}) , \end{aligned} \quad (2.18)$$

which explicitly separates out the momentum-conserving δ -distribution involving the total incoming and outgoing pair momenta \vec{k}'_{12} and \vec{k}_{12} . This operator depends on the spin s_{12} and isospin t_{12} of the pair, on their third components m_{12}^s and m_{12}^t , and on the third component m_{12} of its total angular momentum j_{12} . Besides the photon momenta, it involves the relative momenta \vec{p}'_{12} and \vec{p}_{12} of the in- and outgoing pair. Remember that we exclude charge-transfer or transmutation, *i.e.* impose $m'_{12} = m_{12}$ and $M'_T = M_T$.

The two-nucleon operator is usually represented in terms of two-nucleon partial-wave states with quantum numbers

$$|\alpha_{12}\rangle = |(l_{12} s_{12}) j_{12} m_{12}, t_{12} m_{12}^t\rangle . \quad (2.19)$$

If we now restrict ourselves to the case that O_{12} only depends on the momentum-transfer \vec{q} , but not on \vec{k} (see below), we write it as:

$$\begin{aligned} & \langle \alpha'_{12} \vec{k}'_{12} | \hat{O}_{12} | \alpha_{12} \vec{k}_{12} \rangle = \delta_{m'_{12} m_{12}} \delta^{(3)}(\vec{k}'_{12} - \vec{k}_{12} - \vec{q}) \\ & \quad \times \sum_{m_{12}^s m_{12}^t} \langle l_{12} s_{12} (m_{12} - m_{12}^s) m_{12}^s | j_{12} m_{12} \rangle \langle l'_{12} s'_{12} (m'_{12} - m_{12}^s) m_{12}^s | j'_{12} m'_{12} \rangle \\ & \quad \times \int d\hat{p}'_{12} d\hat{p}_{12} Y_{l'_{12}(m'_{12}-m_{12}^s)}^\dagger(\hat{p}'_{12}) Y_{l_{12}(m_{12}-m_{12}^s)}(\hat{p}_{12}) \\ & \quad \times O_{12}(s'_{12} t'_{12} m'_{12} s_{12} t_{12} m_{12} m_{12}^s m_{12}^t; \vec{p}'_{12}, \vec{p}_{12}; \vec{q}) \\ & \equiv \delta_{m'_{12} m_{12}} \delta^{(3)}(\vec{k}'_{12} - \vec{k}_{12} - \vec{q}) O_{12}^{\alpha'_{12} \alpha_{12}}(p'_{12}, p_{12}) . \end{aligned} \quad (2.20)$$

This must be embedded into the three-nucleon space, just like the one-body operator. Expressed in terms of the spectator momentum, the δ -distribution of the two-nucleon operator takes the form $\delta^{(3)}(\vec{p}_3 - \vec{p}'_3 - \frac{1}{3} \vec{q})$. It is then easy to rewrite the matrix element of \hat{O}_{12} . As for the one-body operator, we introduce an angular integration, evaluate the δ -distribution of the spectator’s three-momentum $\vec{p}'_3 = p'_3 \hat{p}'_3$, and arrive at a lengthy expression used in

the ‘‘traditional’’ approach. As in the one-body case, the new method uses the fact that its sums over quantum numbers factorise, so that we re-arrange the matrix element as:

$$\langle M' | \hat{O}_{12} | M \rangle \equiv \sum_{\alpha'_{12}, \alpha_{12}} \int dp_{12} p_{12}^2 dp'_{12} p_{12}'^2 O_{12}^{\alpha'_{12} \alpha_{12}}(p'_{12}, p_{12}) \rho_{\alpha'_{12} \alpha_{12}}^{M_T, M' M}(p'_{12}, p_{12}; \vec{q}) \ , \quad (2.21)$$

where we define the two-body (transition) density as:

$$\begin{aligned} \rho_{\alpha'_{12} \alpha_{12}}^{M_T, M' M}(p'_{12}, p_{12}; \vec{q}) := & \\ & \sum_{\alpha'(\alpha'_{12})\alpha(\alpha_{12})} \langle j_{12} j_3 m_{12}(M - m_{12}) | J M \rangle \langle j'_{12} j'_3 m'_{12}(M' - m'_{12}) | J' M' \rangle \\ & \times \langle t_{12} t_3 m_{12}^t(M_T - m_{12}^t) | T M_T \rangle \langle t'_{12} t_3 m_{12}^t(M_T - m_{12}^t) | T' M_T \rangle \\ & \times \int dp'_3 p_3'^2 \int d\vec{p}'_3 \psi_{\alpha'}^\dagger(p'_{12} p'_3) \psi_{\alpha}(p_{12} |\vec{p}'_3 + \frac{1}{3}\vec{q}|) \\ & \times \sum_{m_3^s} Y_{l'_3(M' - m'_{12} - m_3^s)}^\dagger(\hat{p}'_3) Y_{l_3(M - m_{12} - m_3^s)}(\widehat{|\vec{p}'_3 + \frac{1}{3}\vec{q}|}) \\ & \times \langle l_3 s_3(M - m_{12} - m_3^s) m_3^s | j_3(M - m_{12}) \rangle \\ & \times \langle l'_3 s_3(M' - m'_{12} - m_3^s) m_3^s | j'_3(M' - m'_{12}) \rangle \ . \end{aligned} \quad (2.22)$$

Here, $\alpha(\alpha_{12})$ is the set of quantum numbers α which characterise the system, for a given set of quantum numbers α_{12} in the (12) subsystem, defined in eq. (2.19). As in the one-body case, the wave functions only enter the final answer through the density. Equations (2.21) and (2.22) make it manifest that not all of the wave function is needed to evaluate the two-body contribution to the matrix element; the relevant numbers are instead the densities $\rho_{\alpha'_{12} \alpha_{12}}^{M_T, M' M}(p'_{12}, p_{12}; \vec{q})$. Once these are known for a particular wave function, evaluating the two-body piece of the Compton amplitude is quite rapid; see discussion in sects. 3.3 and 3.4.

Note that it was not necessary to specify a particular reference frame for the definition of the two-body density since it only depends on the momentum transfer. This is not the case if matrix elements of \hat{O}_{12} in eq. (2.20) also depend on \vec{k}_{12} . An extension to include such boost effects using a multipole expansion analogous to the one-body case of eq. (2.9) is straightforward but not implemented in our present file format.

We see again that the production of two-body densities and their convolution with the two-body kernel factorise, and that the two-body densities can be used quite generally to evaluate matrix elements involving external probes (for now without charge-transfer reactions or boost effects).

The normalisation of the wave function requires the trace of the two-body density at $\vec{q} = 0$ to be given by

$$\delta_{MM'} \stackrel{!}{=} \sum_{\alpha_{12}} \int dp_{12} p_{12}^2 \rho_{\alpha_{12} \alpha_{12}}^{M_T, M' M}(p_{12}, p_{12}; \vec{q} = 0) \ , \quad (2.23)$$

and thus, two-body densities carry units of fm³.

As with the one-body case in sect. 2.3 we can relate this normalisation to a particular example of convoluting two-body densities and operators. Choosing the operator

$$N_{12}^{\alpha'_{12}\alpha_{12}}(p'_{12}, p_{12}) = 3 \delta_{l'_{12}l_{12}} \delta_{s'_{12}s_{12}} \delta_{j'_{12}j_{12}} \delta_{m'_{12}m_{12}} \frac{\delta(p'_{12} - p_{12})}{p_{12}^2} \times \begin{cases} \delta_{m_{12}^t, 1} & \text{for pp} \\ \delta_{m_{12}^t, 0} & \text{for np} \\ \delta_{m_{12}^t, -1} & \text{for nn} \end{cases} \quad (2.24)$$

as O_{12} in eq. (2.21) will yield the pair-form factor, *i.e.* the number of nucleon-pairs at momentum transfer \vec{q} for a given pair-isospin m_{12}^t . Here, we include a convenient factor of $\binom{A=3}{2} = 3$: this is the total number of nucleon pairs in ³He. Computing eq. (2.21) then leads to matrix elements

$$A_M^{M'}(m_{12}^t; \vec{q}) := 3 \sum_{\substack{\alpha_{12} \\ \text{for given } m_{12}}} \int dp_{12} p_{12}^2 \rho_{\alpha_{12}\alpha_{12}}^{M_T, M'M}(p_{12}, p_{12}; \vec{q}) \quad (2.25)$$

which indeed count, for $\vec{q} = 0$, the number of nucleon pairs. In ³He:

$$\lim_{\vec{q} \rightarrow 0} A_M^{M'}(m_{12}^t; \vec{q}) \stackrel{!}{=} \delta_{M'M} \times \begin{cases} 1 & \text{pp pair} & (m_{12}^t = 1) \\ 2 & \text{np pairs} & (m_{12}^t = 0) \\ 0 & \text{nn pairs} & (m_{12}^t = -1) \end{cases} . \quad (2.26)$$

These relations follow from eq. (2.23). In practice, the two-body norm and eq. (2.26) are not strictly fulfilled: the evaluation with densities produces a result that is slightly smaller than the correct number. This is as with the one-body normalisation in eq. (2.17) and happens for the reasons discussed there. We quantify this deviation from the ideal normalisation in sect. 3.3.2.

We close this section by discussing storage for two-body densities. One- and few-body densities all depend of course on the kinematics \vec{q} as well as the spin and isospin of the nucleus itself (and $(K\kappa)$ if so desired). However, the file-size of two-body densities is much larger than for one-body densities. First, two-body densities are subject to a much wider range of quantum numbers of the (12) sub-system. Recall from eq. (2.19) that $\alpha_{12} = [(l_{12}s_{12})j_{12}m_{12}, t_{12}m_{12}^t]$ and analogously for α'_{12} , where $s_{12} \in \{0; 1\}$, $l_{12} \in \{|j_{12} - s_{12}|, \dots, j_{12} + s_{12}\}$, $t_{12} \in \{0; 1\}$, and j_{12} goes up to a value which determines the numerical accuracy and the convergence of the computation; see discussion in sect. 3.3.2. The combinations to be stored are of course reduced by constraints on isospin and angular-momentum couplings to fit the quantum numbers of the target, but even so, there are many more than the corresponding eight quantum-number combinations $(m_3^s m_3^s m_3^t)$ for a one-body density.

However, particularly costly is a dense-enough grid of momenta (p'_{12}, p_{12}) for the two-body density, such that the integration in eq. (2.21) can be performed with sufficient accuracy; for further discussion see sect. 3.4.2. Thus, even with very good compression methods (hdf5 format), two-body densities for ³He reach about 10 MB per probe energy and angle for $j_{12} \leq 1$, about 100 MB for $j_{12} \leq 2$, about 250 MB for $j_{12} \leq 3$, about 750 MB for $j_{12} \leq 4$,

and some 1,400 MB for $j_{12} \leq 5$. These sizes are not exorbitant but can pose storage and memory issues in bulk computations. Files would be reduced to half or quarter of the quoted sizes by taking advantages of symmetry relations; see sect. 2.5.

One should mention that, while the number of allowed quantum numbers can vary quite a bit from nucleus to nucleus, the size of the integration grid for a given accuracy is much less variable. That may lead to an amusing situation in which the *computation* of a two-nucleon density for the spin-0 nucleus ^{12}C is considerably more involved than that of, say, a spin- $\frac{1}{2}$ system like ^7Li —but the *storage* needed for ^{12}C is actually quite a bit smaller. Computing two-body densities scales with powers of A , but storing scales with powers of J .

2.5 Symmetries of Few-Body Densities

We begin with the one-body density, which can be written in a representation-independent operator form as:

$$\rho_{m_3^s m_3^t}^{K\kappa; m_3^s m_3^t M_T, M' M}(\vec{k}, \vec{q}) = \langle M' | \left[|s_3 m_3^s, t_3 m_3^t\rangle e^{i\frac{2}{3}\vec{q}\cdot\vec{r}_3} \left[\vec{p}_3 - \frac{1}{3}\vec{k} \right]^{K\kappa} \langle s_3 m_3^s, t_3 m_3^t | \right] | M \rangle . \quad (2.27)$$

Here, \vec{p}_3 and \vec{r}_3 must be understood as operators. Recall from momentum conservation, eq. (2.12), that $\frac{2}{3}\vec{q} = \vec{p}_3' - \vec{p}_3$ is the momentum transferred to the struck nucleon 3 in relative coordinates. Thus, $e^{i\frac{2}{3}\vec{q}\cdot\vec{r}_3}$ is the momentum-transfer operator in the nucleon cm frame. $[\vec{a}]^{K\kappa}$ represents the κ th component of the irreducible tensor of rank K constructed from the vector \vec{a} ; see eq. (2.9). The projection operator in the spin-space of particle 3 defines that particle's spin projections. This is combined with a projector that enforces a specific isospin for nucleon 3. There is also an implicit identity operator in the (12) piece of the three-body Hilbert space that is not written in eq. (2.27). Inserting complete sets of states $|p_{12}\alpha_{12}\rangle|p_3 l_3 m_3^l\rangle|s_3 m_3^s\rangle$ and $|p_{12}p_3\alpha\rangle$ between the initial state and the operator so that the wave function is evaluated in the Jacobi α representation and then doing the same in the final state, verifies that eq. (2.27) is equivalent to eq. (2.14).

2.5.1 Time Reversal

As the densities are generated from strong and electromagnetic interactions, they are time-reversal invariant. Under this symmetry, states in which angular momenta are coupled to a total j and projection m_j transform as [45]

$$\mathcal{T}|j, m_j\rangle = (-1)^{j+m_j} |j, -m_j\rangle . \quad (2.28)$$

Likewise, when an operator T is multipole-expanded into angular momentum (LM), time-reversal invariance requires (*cf.* properties of spherical harmonics)

$$T_{L,-M} = (-1)^M T_{LM}^\dagger . \quad (2.29)$$

As this symmetry will also be exploited in eq. (3.12) for two-body Compton matrix elements, we note that photon helicity states transform thus as

$$\mathcal{T}|\lambda\rangle = (-1)^\lambda |-\lambda\rangle . \quad (2.30)$$

These symmetries imply that one-body densities for arbitrary-spin targets $J = J'$ fulfil an exact relation when the sign of all spin-projection quantum numbers is reversed:

$$\rho_{(-m_3^{s'})(-m_3^s)}^{K(-\kappa);m_3^t M_T,(-M')(-M)}(\vec{k}, \vec{q}) = (-1)^{(M'-M)+(m_3^{s'}-m_3^s)+\kappa} \rho_{m_3^{s'} m_3^s}^{K\kappa;m_3^t M_T, M' M}(\vec{k}, \vec{q}) . \quad (2.31)$$

This cuts in half the number of one-body densities which need to be computed, and hence the computational effort and the storage requirement—albeit the latter is not a big deal for one-body densities.

Similarly, two-body densities obey (we do not consider multipole expansions in \vec{k}_{12}):

$$\begin{aligned} & \rho_{\alpha'_{12}(-m'_{12})\alpha_{12}(-m_{12})}^{M_T,(-M')(-M)}(p'_{12}, p_{12}; \vec{q}) \\ &= (-1)^{(M'-M)+j'_{12}+j_{12}+(m'_{12}-m_{12})+l'_{12}+l_{12}} \rho_{\alpha'_{12}(m_{12})\alpha_{12}(m_{12})}^{M_T, M' M}(p'_{12}, p_{12}; \vec{q}) , \end{aligned} \quad (2.32)$$

where $\alpha_{12}(-m_{12})$ is α_{12} of eq. (2.19) with the sign of m_{12} reversed.

2.5.2 Hermiticity and Parity

Another symmetry of two-body densities guarantees that matrix elements generated from them are Hermitean, namely the interchange of primed (outgoing) and unprimed (incoming) quantum numbers and momenta:

$$\rho_{\alpha'_{12}\alpha'_{12}}^{M_T, M' M'}(p_{12}, p'_{12}; \vec{q}) = (-1)^{l'_{12}+l_{12}} \rho_{\alpha'_{12}\alpha_{12}}^{M_T, M' M}(p'_{12}, p_{12}; \vec{q}) . \quad (2.33)$$

To derive it, we first use the fact that the densities are real because there are no open channels, and take the complex conjugate on both sides. Then, we shift the integration variable in eq. (2.22), adjusting \vec{p}'_3 to $\vec{p}'_3 - \frac{\vec{q}}{6}$, so that the integral over \vec{p}'_3 is manifestly symmetric under $\vec{q} \rightarrow -\vec{q}$. After exchanging all primed and unprimed variables, except for the integration variable \vec{p}'_3 , the expression contains the integral

$$\begin{aligned} & \int dp'_3 p_3'^2 \int dp'_3 \psi_\alpha(p_{12}|\vec{p}'_3 - \frac{1}{6}\vec{q}|) \psi_{\alpha'}^\dagger(p'_{12}|\vec{p}'_3 + \frac{1}{6}\vec{q}|) \\ & \times Y_{l_3(M-m_{12}-m_3^s)}(\widehat{\vec{p}'_3 - \frac{1}{6}\vec{q}}) Y_{l'_3(M'-m'_{12}-m_3^s)}^\dagger(\widehat{\vec{p}'_3 + \frac{1}{6}\vec{q}}) . \end{aligned} \quad (2.34)$$

Changing integration variable once again, $\vec{p}'_3 \rightarrow -\vec{p}'_3$, and using the parity of the spherical harmonics, $Y_{lm}(\Omega) = (-1)^l Y_{lm}(-\Omega)$, to reverse their arguments, reveals that this is the same integral as in eq. (2.22), but with pre-factor $(-1)^{l_3+l'_3}$. Since the parity of the ground state of the nucleus is unchanged by the reaction, we use $(-1)^{l_3+l_{12}} = (-1)^{l'_3+l'_{12}}$ to arrive at the identity (2.33).

For one-body densities, the angular integral in eq. (2.14) can likewise be rewritten by changing the integration variable $\vec{p}_3 \rightarrow -\vec{p}_3$ and using the parity of the spherical harmonics. This produces the same expression, but with an additional factor $(-1)^{l_3+l'_3+K}$ and the signs of \vec{q} and \vec{k} reversed. In the one-body case, l_{12} is unchanged by the interaction with the

external probe so $(-1)^{l_3} = (-1)^{l'_3}$. As both are integers, we arrive at the parity relation for one-body densities:

$$\rho_{m_3^s m_3^s}^{K\kappa; m_3^t M_T, M'M}(\vec{q}, \vec{k}) = (-1)^K \rho_{m_3^s m_3^s}^{K\kappa; m_3^t M_T, M'M}(-\vec{q}, -\vec{k}) . \quad (2.35)$$

This identity is, however, of limited use, since we always choose \vec{k} in the positive \hat{z} direction. It merely indicates that for even (odd) K , the density is even (odd) when reversing \vec{q} and \vec{k} . In particular, at $\vec{q} = \pm\vec{k}$, densities must be zero for odd K , or their derivatives with respect to \vec{q} and \vec{k} must be zero for even K .

It does tell us, though, that in the case $K = \kappa = 0$ the density is even in \vec{q} , and therefore real; see eq. (2.22). This leads to a Hermiticity relation for $K = \kappa = 0$ that is the one-body version of eq. (2.33). It is obtained by taking the Hermitean conjugate of eq. (2.27) to get:

$$\rho_{m_3^s m_3^s}^{00; m_3^t M_T, M'M}(\vec{q}) = \rho_{m_3^s m_3^s}^{00; m_3^t M_T, MM'}(-\vec{q}) , \quad (2.36)$$

where we used that the density for $K = \kappa = 0$ does not depend on the initial-state momentum of the nucleus, $-\vec{k}$. Invoking eq. (2.35) then produces:

$$\rho_{m_3^s m_3^s}^{00; m_3^t M_T, M'M}(\vec{q}) = \rho_{m_3^s m_3^s}^{00; m_3^t M_T, MM'}(\vec{q}) . \quad (2.37)$$

2.5.3 Flipping Symmetry

So far, the symmetries discussed in this section hold for a target of arbitrary target spin J . Now, we specialise to the case $J = \frac{1}{2}$ and elucidate an additional symmetry which relates the transition density from states with a “wrong-spin” nucleon, *i.e.* a nucleon whose spin is anti-aligned with the target spin, to states where the same nucleon has its spin aligned with that of the nucleus. The following relations then go beyond the time-reversal relation (2.31):

$$\begin{aligned} \rho_{(-M')M}^{00; m_3^t M_T, M'M}(\vec{q}) &= \rho_{M'M}^{00; m_3^t M_T, (-M')M}(\vec{q}) , \\ \rho_{M'(-M)}^{00; m_3^t M_T, M'M}(\vec{q}) &= \rho_{M'M}^{00; m_3^t M_T, M'(-M)}(\vec{q}) . \end{aligned} \quad (2.38)$$

The presence of a wrong-spin nucleon is the key to proving them. We begin with the operator form of the density, eq. (2.27), and choose to work in the basis

$$|p_{12} r_3(j_{12} l_3) \ell_{123}, \mu_{123}\rangle |s_3 m_3^s\rangle . \quad (2.39)$$

Notice that this is the only instance in this article where we employ eigenstates of the radial coordinate r_3 of the 3rd particle, and not momentum eigenstates. Here, $\vec{\ell}_{123} \equiv \vec{j}_{12} + \vec{l}_3$ is the total angular momentum of everything in the nucleus apart from the spin of the third nucleon, so $\ell_{123} = \vec{J} - \vec{s}_3$. Since $J = s_3 = \frac{1}{2}$ in the case of interest, $\ell_{123} = 1$ or 0 .

Let us now evaluate the density for an initial state with a “wrong spin” $M = -m_3^s = \pm\frac{1}{2}$. Since then $\mu_{123} = M - m_3^s = \pm 1$, only pieces of the initial-state ${}^3\text{He}$ wave function with $\ell_{123} = 1$ can contribute. Furthermore, parity conservation ensures that the operator $e^{i\frac{2}{3}\vec{q}\cdot\vec{r}_3}$

only changes l_3 by $0, 2, 4, \dots$, so transitions from $\ell_{123} = 1$ to $\ell_{123} = 0$ do not occur. The density can then be written as:

$$\begin{aligned} \rho_{M'(-M)}^{00; m_3^t M_T, M'M}(\vec{q}) &= \int dp_{12} p_{12}^2 \int dr_3 r_3^2 \langle M' | \left[|s_3, M'; m_3^t\rangle |p_{12} r_3 (j_{12} l_3) 1, 0\rangle \right. \\ &\quad \left. \times \langle (j_{12} l_3) 1, 0 | e^{i\frac{2}{3}\vec{q}\cdot\vec{r}_3} |(j_{12} l_3) 1, 2M\rangle \langle (j_{12} l_3) 1, 2M | \langle s_3, -M; m_3^t | \right] |M\rangle . \end{aligned} \quad (2.40)$$

That is, for transitions involving a wrong-spin nucleon, only the $\ell_{123} = 1$ piece of the wave function is needed in both the initial and final state. We then employ the time-reversal properties of the $|\ell_{123} \mu_{123}\rangle$ states, and of spin-half states, to derive the matrix-element relations:

$$\begin{aligned} \left[\langle p_{12} r_3 (j_{12} l_3) 1, \pm 1 | \langle s_3, -M | \right] |M\rangle &= - \left[\langle p_{12} r_3 (j_{12} l_3) 1, \mp 1 | \langle s_3, M | \right] | -M\rangle , \\ \langle (j_{12} l_3) 1, 0 | e^{i\frac{2}{3}\vec{q}\cdot\vec{r}_3} |(j_{12} l_3) 1, 1\rangle &= - \langle (j_{12} l_3) 1, 0 | e^{i\frac{2}{3}\vec{q}\cdot\vec{r}_3} |(j_{12} l_3) 1, -1\rangle . \end{aligned} \quad (2.41)$$

The second equality in eq. (2.38) follows immediately. The first can be proven through the same argument, applied instead in the final state.

We will quote the relatively straightforward generalisation of eq. (2.38) to the case of a nucleus of arbitrary spin in a future publication.

2.5.4 Closing Comments on Symmetries of the Densities

In the one-body case eq. (2.31) reduces the number of independent transition densities by half, e.g., in ${}^3\text{He}$ from 16 to 8 for $K = \kappa = 0$ and a specific m_3^t . For $J = \frac{1}{2}$ nuclei, eq. (2.38) then relates two of the remaining 8, with eq. (2.37) removing one more. This leaves us with 5 independent transition densities at a given \vec{q} and m_3^t for $K = \kappa = 0$. In fact, since eq. (2.40) expresses the density in terms of a particular irreducible representation of a spherical tensor, the Wigner-Eckart theorem can be used to further reduce the number of independent one-body ($K = \kappa = 0$) transition densities at a particular value of \vec{q} to three, but we do not develop those two additional relations here. In fact, we do not use any of the symmetry relations discussed in this section to reduce storage requirements for the one-body density. These are very small anyway, and keeping all $(2K + 1) * 16$ densities per isospin for a given K allows us to check the numerical accuracy of our results.

We finish this section with two notes. First, other variants of the symmetry relations can be written, but they reduce to those above when one uses that $l'_{12} + l'_{12} + s'_{12}$ and $t_{12} + l_{12} + s_{12}$ must be odd (Pauli principle); that either both $l_{12} + l_3$ and $l'_{12} + l'_3$ are even, or both are odd (parity of state); and that all these quantum numbers are integers. Second, as exemplified in the argument that justifies eq. (2.33), in the presence of open thresholds the symmetry relations of this section would include complex conjugation. However, we have omitted complex conjugation in the versions we write here, instead presenting them for the purely real densities we have computed: there are no open channels in our calculation.

3 Convergence and Comparisons

We now provide evidence that the new method speeds up the calculation of matrix elements; that its results converge numerically; and that the converged results agree and indeed improve both numerically and in efficiency over those of the “traditional” approach. To that end, we consider in detail matrix elements which enter in Compton scattering on ${}^3\text{He}$ in the χEFT calculation, the specifics of which are not especially relevant in the present context. We only use this particular process to illustrate and benchmark the method.

3.1 Matrix Elements for Elastic Compton Scattering

3.1.1 Target Matrix Elements

The matrix element of the $\gamma{}^3\text{He}$ amplitude depends on the spin projections M and M' of the incoming and outgoing nucleus onto the z -axis and on the helicities λ and λ' of the incident and outgoing photons with polarisations $\vec{\epsilon}$ and $\vec{\epsilon}'$, respectively. Using permutations, symmetries and the same notation as in sects. 3.1.2 and 3.1.3, it is:

$$A_{M\lambda}^{M'\lambda'}(\vec{k}, \vec{q}) = 3 \langle M' | \left[\hat{O}_3^{\lambda'\lambda}(\vec{k}, \vec{q}) + \hat{O}_{12}^{\lambda'\lambda}(\vec{k}, \vec{q}) \right] | M \rangle , \quad (3.1)$$

where the symmetry factor arises again because one of $A = 3$ indistinguishable nucleons, or one of $\binom{A=3}{2} = 3$ indistinguishable nucleon-pairs can be struck.

The amplitude is evaluated in the cm frame of the photon-nucleus system, where no energy is transferred. In Compton scattering, the incident-probe momentum \vec{k} and the momentum-transfer \vec{q} which we used to characterise the transition densities are traditionally replaced by the energy of both incident and outgoing photon, $\omega = |\vec{k}| = |\vec{k}'|$ and by the scattering angle θ for the outgoing photon:

$$\cos \theta = 1 - \frac{\vec{q}^2}{2\omega^2} . \quad (3.2)$$

From now on, we therefore discuss results using the variables (ω, θ) of the cm frame.

3.1.2 One-Body Operators

In the cm frame of the photon-nucleon collision, the amplitude for Compton scattering from a single nucleon is parametrised by a basis of six operators, each of which is multiplied by an “invariant function” A_i , $i = 1, \dots, 6$. These depend on the photon energy ω and scattering angle $\theta = \arccos(\hat{\vec{k}} \cdot \hat{\vec{k}}')$, as well as the struck nucleon’s isospin. The object traditionally labelled $T(\omega, \cos \theta)$ in the Compton literature is, in the notation for one-body amplitudes

established in sect. 2.3:

$$\begin{aligned}
O_3^{\lambda'}(m_3^{s'} m_3^s m_3^t; \vec{k}, \vec{q} = \vec{k} - \vec{k}') = \\
\langle m_3^{s'} | \left[A_1(\omega, \cos \theta) (\vec{\epsilon}'^\dagger \cdot \vec{\epsilon}) + A_2(\omega, \cos \theta) (\vec{\epsilon}'^\dagger \cdot \hat{k}) (\vec{\epsilon} \cdot \hat{k}') \right. \\
+ i A_3(\omega, \cos \theta) \vec{\sigma} \cdot (\vec{\epsilon}'^\dagger \times \vec{\epsilon}) + i A_4(\omega, \cos \theta) \vec{\sigma} \cdot (\hat{k}' \times \hat{k}) (\vec{\epsilon}'^\dagger \cdot \vec{\epsilon}) \quad (3.3) \\
+ i A_5(\omega, \cos \theta) \vec{\sigma} \cdot \left[(\vec{\epsilon}'^\dagger \times \hat{k}) (\vec{\epsilon} \cdot \hat{k}') - (\vec{\epsilon} \times \hat{k}') (\vec{\epsilon}'^\dagger \cdot \hat{k}) \right] \\
\left. + i A_6(\omega, \cos \theta) \vec{\sigma} \cdot \left[(\vec{\epsilon}'^\dagger \times \hat{k}') (\vec{\epsilon} \cdot \hat{k}') - (\vec{\epsilon} \times \hat{k}) (\vec{\epsilon}'^\dagger \cdot \hat{k}) \right] \right] | m_3^s \rangle .
\end{aligned}$$

The Kronecker- δ enforces charge conservation in electromagnetic interactions.

Upon inspection of eq. (3.3), one infers that, for given photon kinematics, the only independent matrix elements that actually need to be computed to reconstruct the one-body Compton amplitude are those of the spin-space operators which act on a single nucleon N:

$$\sigma_\mu^{(N)} := (\sigma_0^{(N)} \equiv \mathbb{1}^{(N)}, \sigma_x^{(N)}, \sigma_y^{(N)}, \sigma_z^{(N)}) . \quad (3.4)$$

Therefore, the analysis of sect. 3 compares one-body matrix elements with insertions of these spin operators with momentum transfer \vec{q} and no dependence on \vec{k} (*i.e.* multipolarity $K = \kappa = 0$) between ${}^3\text{He}$ states:

$$A_M^{M'}(\sigma_\mu^{(N)}; \vec{q}) := \langle M' | 3 \sigma_\mu^{(N)} e^{i\frac{2}{3}\vec{q}\cdot\vec{r}_3} | M \rangle , \quad (3.5)$$

where we inserted again a factor of 3 because the nucleons inside the $A = 3$ nucleus are indistinguishable. For the $\mu = 0$ component, this is just the matrix element of the nucleon-number operator N_3 of eq. (2.15) which at $\vec{q} = 0$ yields the normalisation of the one-body density in eq. (2.17):

$$A_M^{M'}(\sigma_0^{(N)}; \vec{q}) \equiv \langle M' | 3 \sigma_0^{(N)} e^{i\frac{2}{3}\vec{q}\cdot\vec{r}_3} | M \rangle \equiv 3 \sum_{m_3^s} \rho_{m_3^s m_3^s}^{(K=0)(\kappa=0); (m_3^t = \pm\frac{1}{2})(M_T = \frac{1}{2}), M' M}(\vec{k}, \vec{q}) . \quad (3.6)$$

The matrix elements of the spin insertions are not independent. They are related to one another by rotations (and boosts) and by time reversal. The connection between the symmetries of the densities derived in sec. 2.5 and these relations the matrix elements (3.5) is discussed in app. B.

3.1.3 Two-Body Operators

The one-body case focused on the 8 insertion operators $\sigma_\mu^{(N)}$. In the two-body case, we would face 16 two-nucleon combinations of nucleon-1-times-nucleon-2 spin-space operators

$$\{\mathbb{1}, \vec{\sigma}_1\} \otimes \{\mathbb{1}, \vec{\sigma}_2\} = \mathbb{1} \oplus \vec{\sigma}_1 \cdot \vec{\sigma}_2 \oplus \vec{\sigma}_1 \oplus \vec{\sigma}_2 \oplus [\vec{\sigma}_1 \times \vec{\sigma}_2] \oplus \left[\sigma_1^i \sigma_2^j - \frac{1}{3} \delta^{ij} \vec{\sigma}_1 \circ \vec{\sigma}_2 \right] \quad (3.7)$$

times 4 initial- and final-state combinations of the ${}^3\text{He}$ spin, for each isospin (t_{12}, m_{12}^t) of the pair. The analogous study would provide an overabundance of detail, in particular since it will turn out that in Compton scattering, significant two-body contributions enter only in matrix elements $M' = M$ which do not change the ${}^3\text{He}$ spin. Instead, we simply discuss results for the entire $\mathcal{O}(e^2\delta^2)$ two-body operator, *i.e.* for the matrix elements $A_{M,\lambda}^{M',\lambda'}(\vec{k}, \vec{q})$ characterised by the helicities λ, λ' of the incoming and outgoing photons.

In Compton scattering, the first nonzero contributions to the two-body kernel in χEFT enters at N²LO [$\mathcal{O}(e^2\delta^2)$], when both photons couple to the same charged pion-exchange current, see fig. 4. They were first computed in ref. [38], where full expressions can be found, and were also used in all subsequent ${}^3\text{He}$ publications [24–28]. All these two-body diagrams only contribute for np pairs, *i.e.* they all contain an isospin factor of $\tau^{(1)} \cdot \tau^{(2)} - \tau_z^{(1)}\tau_z^{(2)}$. However, one distinction between ${}^3\text{He}$ and the deuteron is that for $A = 3$, pairs with both isospin $t_{12} = 0$ and 1 must be counted, so the summation over quantum numbers of the (12) subsystem is different. There are no two-body corrections at $\mathcal{O}(e^2\delta^3)$ [N³LO], even when the $\Delta(1232)$ excitation is treated as an explicit degree of freedom. Finally, we list the values of the parameters of the interaction kernels in Compton scattering on the deuteron and ${}^3\text{He}$ [6, 24–28, 47]. Since the photons couple only to the charged component of the pion-exchange currents, we use the charged-pion mass $m_\pi = 139.6$ MeV. The pion-decay constant is $f_\pi = 92.42$ MeV; the pion-nucleon coupling $g_A = 1.267$; the fine structure constant $\alpha_{EM} = \frac{1}{137.036}$; and $1 = \hbar c = 197.327$ MeV fm.

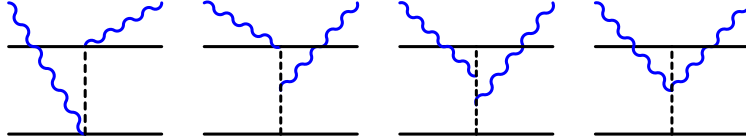


Figure 4: (Colour online) The Compton kernel for two-body contributions at N²LO [$\mathcal{O}(e^2\delta^2)$]; crossed and permuted diagrams not displayed.

3.2 Choices: Interactions, Kinematic Range and Criteria

We choose two sets of 2N and 3N interactions to generate the one- and two-body densities (and the wave functions for the “traditional” approach). The AV18 NN model interaction [20], supplemented by the Urbana-IX 3N interaction (3NI) [21], is relatively “hard” and thus numerically often somewhat more challenging, while concurrently being local in coordinate space, so that a wide variety of computational approaches can be employed. This makes it a popular choice for testing new methods. In contradistinction, the chiral Idaho N³LO interaction for the 2N system at cutoff 500 MeV [22] with the $\mathcal{O}(Q^3)$ χEFT 3N interaction in variant “b” of ref. [23], is also local but considerably softer. Both capture the correct long-distance physics of one-pion exchange and reproduce both the NN scattering data and the experimental value of the triton and ${}^3\text{He}$ binding energies well.

These are of course only two out of a number of modern, sophisticated potentials. For the purpose of this presentation, our choice is dictated by the fact that both are already

available in the “traditional” code, so that they happen to be the ones most used in ${}^3\text{He}$ Compton scattering [24–28]. In sect. 3.4, we will thus also be able to compare the results of the “traditional” and “density” approach. We believe that they provide sufficiently different, realistic numerical challenges.

As discussed in the Introduction and sect. 2.1, we concentrate on energies $50 \text{ MeV} \lesssim \omega \lesssim 120 \text{ MeV}$, well below the pion-production threshold, where rescattering effects are small and where experiments are most likely to be conducted, see also detailed discussions in refs. [6, 28]. In this range, extremes of energies and angles are of particular interest. At forward angles, momentum transfers are small, and one is more sensitive to components of the densities or wave functions which are nearly diagonal, $M' = M$. Matrix elements at back-angles (large momentum transfers) tend to be more sensitive to off-diagonal components. Smaller energies probe long-range components, while higher energies are more sensitive to short-distance pieces of the wave function and the “softness” of the NN interactions. On the other hand, one should avoid the special symmetries which dominate the cross sections at 0° and 180° . We therefore illustrate our results for two extreme (but not too extreme) choices: $(\omega = 50 \text{ MeV}, \theta = 30^\circ)$, where the momentum transfer is according to eq. (3.2) given by $|\vec{q}| = \sqrt{2\omega^2(1 - \cos\theta)} = 25.9 \text{ MeV}$; and $(\omega = 120 \text{ MeV}, \theta = 165^\circ)$, where $|\vec{q}| = 237.9 \text{ MeV}$. Results at other energies and angles do not change our conclusions.

We use two convergence and comparison criteria: the magnitude of the relative deviation for a given matrix element ($M'M$) at fixed energy, angle and operator identifier β :

$$\frac{|\Delta A_M^{M'}(\beta; \vec{k}, \vec{q})|}{|A_M^{M'}(\beta; \vec{k}, \vec{q})|} ; \quad (3.8)$$

and the size of the deviation of that matrix element relative to the largest of all magnitudes of the matrix elements at the same energy and angle, over a set of spin projections and operator identifiers:

$$\frac{|\Delta A_M^{M'}(\beta; \vec{k}, \vec{q})|}{\max_{\{M', M; \beta\}} |A_M^{M'}(\beta; \vec{k}, \vec{q})|} . \quad (3.9)$$

For one-body matrix elements, β is both the label μ and the particle identifier of the spin matrix $\sigma_\mu^{(N)}$; for two-body densities, it is the set of photon helicities (λ', λ) in the Compton kernel.

Finally, while details of runtimes to produce one- and two-body densities are of course highly dependent on processor and motherboard, we report them based on our experience on the JURECA cluster of the Jülich Supercomputing Centre (Jülich, Germany). The runtime magnitudes quoted for the “traditional” approach and for the convolution step of the density approach were found on a single core of a typical 7th-generation i7-4770 with 8 cores at 3.4GHz. Ratios of runtimes should be fairly processor-independent.

3.3 Convergence of Matrix Elements in the Densities Method

The results we now present are fully converged in the radial and angular integrations, to a relative deviation of better than 10^{-4} . We therefore consider now the more interesting

question of convergence with respect to the number of partial waves.

First, though, we notice that the $A = 3$ system is a special case. One can consider convergence with respect to the total angular momentum j_{12} of the pair, or with respect to j_3 , that of the “outermost” nucleon. The two criteria are however not interchangeable. Specifying the quantum numbers and momenta of the (12) pair and of the nucleus as a whole determines a range of quantum numbers of the third nucleon, but not a unique value. Imposing a maximum j_{12} or j_3 leads therefore to differently truncated model spaces, but both do of course converge to the same value as more partial waves are included. We choose to examine convergence in j_{12} for both one- and two-body matrix elements.

These convergence studies on ${}^3\text{He}$ also provide experience for upcoming, more computationally intensive computations. In ${}^4\text{He}$ and heavier nuclei, convergence of matrix elements is potentially more naturally discussed using the total angular momentum of the system of “active” nucleons. That is still j_{12} for two-body densities, and $j_{1\dots n}$ for a system of nucleons ($1\dots n$) which are all “active”, *i.e.* interact with the probe ($n > 1$). For one-body matrix elements, on the other hand, one would consider j_A of the “active” nucleon, and not $j_{1\dots(A-1)} \rightarrow j_{12}$ as we do for $A = 3$.

3.3.1 Convergence of One-Body Matrix Elements

We first turn to the results for the one-body densities in ${}^3\text{He}$. Here, j_{12} is the relative total angular momentum between the *spectators* of the Compton process. We use a sequence $j_{12} \leq 1, 2, 3, 4, 5$, for which typical runtimes to produce the one-body densities should roughly increase with the square of the number of channels α_{12} probed. However, actual runtimes scale significantly better, indicating that preparations including I/O take most of the time. Compared to the production time for a density with $j_{12} \leq 1$, one with $j_{12} \lesssim 2$ takes only about 1.2 times as long, compared to a factor 4 from the rough estimate; 1.3 times for $j_{12} \lesssim 3$ (estimate: 7 times); 1.6 times for $j_{12} \lesssim 4$ (estimate: 14 times); and 1.8 times for $j_{12} \lesssim 5$ (estimate: 20 times). The latter takes less than 3 s on JURECA, using 8 nodes with 68 cores each, or about 20 CPU-minutes. With densities in hand, computing the matrix elements of $\sigma_\mu^{(N)}$, eq. (3.5), in the ${}^3\text{He}$ ground state only involves summations over quantum numbers and is therefore nearly instantaneous. As σ_y is imaginary in our representation, we show the matrix elements for $i\sigma_y$, which are real.

As discussed in sects. 2.3 and 3.1.2, the matrix elements are normalised following eq. (2.17) such that an insertion of $3\sigma_0^{(p)}$ ($3\sigma_0^{(n)}$) at $\omega = 0$ simply counts the number of protons (neutrons) in the target, *i.e.* the result should be $2\delta_{M'M}$ ($\delta_{M'M}$). These relations are approached from below. We produced densities at zero momentum-transfer and confirmed that at $j_{12} \leq 5$, the relative difference is $< 0.41 \times 10^{-3}$ for the proton and $< 0.88 \times 10^{-3}$ for the neutron when one uses the chiral Idaho potential, or $< 1.5 \times 10^{-3}$ for the proton and $< 3.3 \times 10^{-3}$ for the neutron when one uses AV18+UIX. In either case, a relative accuracy of $< 7 \times 10^{-3}$ for the normalisation of the one-body density is already achieved for $j_{12} \leq 2$.

Tables 1 and 2 show the convergence pattern and converged values of those 5 matrix elements for $M = \pm\frac{1}{2}$, $M' = \frac{1}{2}$ which are nonzero and not equal to any others. By time-reversal invariance and rotational symmetry, the other 11 matrix elements are zero or equal

$$\omega = 50 \text{ MeV}, \theta = 30^\circ$$

insertion		proton					neutron					
σ_μ	$\{M', M\}$	value	$1 - \frac{j_{12} \leq 1}{j_{12} \leq 5}$	$1 - \frac{j_{12} \leq 2}{j_{12} \leq 5}$	$1 - \frac{j_{12} \leq 3}{j_{12} \leq 5}$	$1 - \frac{j_{12} \leq 4}{j_{12} \leq 5}$	value	$1 - \frac{j_{12} \leq 1}{j_{12} \leq 5}$	$1 - \frac{j_{12} \leq 2}{j_{12} \leq 5}$	$1 - \frac{j_{12} \leq 3}{j_{12} \leq 5}$	$1 - \frac{j_{12} \leq 4}{j_{12} \leq 5}$	
Idaho N ³ LO+3NFb	σ_0	$\{\frac{1}{2}, \frac{1}{2}\}$	1.9806	1.9%	0.6%	0.2%	0.1%	.9914	4.3%	0.5%	0.4%	0.0%
	σ_x	$\{\frac{1}{2}, -\frac{1}{2}\}$	-.0415	-3.7%	3.9%	-1.0%	0.4%	.8821	1.3%	0.1%	0.2%	-0.0%
	$i\sigma_y$	$\{\frac{1}{2}, -\frac{1}{2}\}$	-.0392	-4.0%	4.1%	-1.0%	0.4%	.8822	1.3%	0.1%	0.2%	-0.0%
	σ_z	$\{\frac{1}{2}, \frac{1}{2}\}$ $\{\frac{1}{2}, -\frac{1}{2}\}$	-.0393 .0006	-4.0% 2.1%	4.1% 1.4%	-1.0% 0.1%	0.4% 0.1%	.8822 .0000	1.3% 91.5%	0.1% 1.4%	0.2% 6.7%	-0.0% -0.8%
AV18+UIX	σ_0	$\{\frac{1}{2}, \frac{1}{2}\}$	1.9790	2.6%	1.2%	0.4%	0.2%	.9893	5.5%	1.0%	0.9%	0.0%
	σ_x	$\{\frac{1}{2}, -\frac{1}{2}\}$	-.0548	9.2%	9.4%	1.4%	1.8%	.8616	0.6%	0.1%	0.1%	-0.0%
	$i\sigma_y$	$\{\frac{1}{2}, -\frac{1}{2}\}$	-.0527	9.4%	9.7%	1.4%	1.9%	.8617	0.6%	0.1%	0.1%	-0.0%
	σ_z	$\{\frac{1}{2}, \frac{1}{2}\}$ $\{\frac{1}{2}, -\frac{1}{2}\}$	-.0529 .0005	9.4% 2.5%	9.6% 1.4%	1.4% 0.2%	1.9% 0.0%	.8617 .0000	0.6% 95.6%	0.1% 2.3%	0.1% 9.0%	-0.0% -1.4%

Table 1: Convergence of the one-body matrix elements $A_M^{M'}(\sigma_\mu^{(N)}; \vec{q})$ of eq. (3.5) in ${}^3\text{He}$ with insertions $3\sigma_\mu^{(N)}$ for the proton and neutron, and for potentials Idaho N³LO+3NFb and AV18+UIX in the “density” approach from $j_{12} \leq 1$ up to $j_{12} \leq 5$ at $\omega = 50 \text{ MeV}, \theta = 30^\circ$, where mostly diagonal matrix elements $M' = M$ are probed. The “value” column gives the results summed up to $j_{12} = 5$ in dimensionless units, normalised as in eq. (2.17). Relative differences for sums to lower maximum j_{12} , as defined in eq. (3.8), are shown in the subsequent columns. Only those 5 matrix elements which are independent and non-zero are shown. Appendix B describes how time-reversal invariance relates these to the other 11. See text for further details.

to these, see app. B for further discussion. Those with $M' = -\frac{1}{2}$ follow from eq. (2.28) via a relation which is numerically nearly perfectly satisfied:

$$A_{-M}^{-M'}(\sigma_\mu^{(N)}; \vec{q}) = (-1)^{M'-M+\mu} A_M^{M'}(\sigma_\mu^{(N)}; \vec{q}) . \quad (3.10)$$

Furthermore, the proofs of eqs. (B.8), (B.9) and (B.11) in the appendix show that

$$\begin{aligned} A_{\pm\frac{1}{2}}^{\mp\frac{1}{2}}(\sigma_0^{(N)}; \vec{q}) &= 0 = A_{\pm\frac{1}{2}}^{\pm\frac{1}{2}}(\sigma_y^{(N)}; \vec{q}) \\ A_{\pm\frac{1}{2}}^{\pm\frac{1}{2}}(\sigma_x^{(N)}; \vec{q}) &= A_{\pm\frac{1}{2}}^{\mp\frac{1}{2}}(\sigma_z^{(N)}; \vec{q}) , \end{aligned} \quad (3.11)$$

each of which is fulfilled to better than 10^{-9} .

We note that the progression of the convergence is not monotonic as some wave function components only contribute for sufficiently high j_{12} . However, the computations are clearly converged in j_{12} even at the higher energy and momentum transfer examined in table 2.

$$\omega = 120 \text{ MeV}, \theta = 165^\circ$$

insertion		proton				neutron						
σ_μ	$\{M', M\}$	value	$1 - \frac{j_{12} \leq 1}{j_{12} \leq 5}$	$1 - \frac{j_{12} \leq 2}{j_{12} \leq 5}$	$1 - \frac{j_{12} \leq 3}{j_{12} \leq 5}$	$1 - \frac{j_{12} \leq 4}{j_{12} \leq 5}$	value	$1 - \frac{j_{12} \leq 1}{j_{12} \leq 5}$	$1 - \frac{j_{12} \leq 2}{j_{12} \leq 5}$	$1 - \frac{j_{12} \leq 3}{j_{12} \leq 5}$	$1 - \frac{j_{12} \leq 4}{j_{12} \leq 5}$	
Idaho N ³ LO+3NFb	σ_0	$\{\frac{1}{2}, \frac{1}{2}\}$.9973	1.8%	0.6%	0.1%	0.0%	.5443	3.7%	0.4%	0.3%	0.0%
	σ_x	$\{\frac{1}{2}, -\frac{1}{2}\}$.0381	3.9%	-1.2%	0.8%	-0.1%	.4801	1.5%	0.2%	0.2%	-0.0%
	$i\sigma_y$	$\{\frac{1}{2}, -\frac{1}{2}\}$.0400	3.8%	-1.1%	0.7%	-0.1%	.4801	1.5%	0.2%	0.2%	-0.0%
	σ_z	$\{\frac{1}{2}, \frac{1}{2}\}$	-.0700	0.8%	2.4%	-0.4%	0.1%	.4748	0.7%	0.2%	0.1%	0.0%
		$\{\frac{1}{2}, -\frac{1}{2}\}$.0145	1.9%	1.1%	0.0%	0.0%	.0007	74.5%	-1.0%	3.2%	-0.4%
AV18+UIX	σ_0	$\{\frac{1}{2}, \frac{1}{2}\}$	1.0377	3.0%	1.4%	0.5%	0.2%	.5681	5.7%	1.0%	0.9%	0.0%
	σ_x	$\{\frac{1}{2}, -\frac{1}{2}\}$.0220	-14.3%	-14.1%	-1.5%	-2.9%	.4830	0.6%	0.2%	0.2%	-0.0%
	$i\sigma_y$	$\{\frac{1}{2}, -\frac{1}{2}\}$.0238	-13.1%	-13.0%	-1.4%	-2.7%	.4830	0.6%	0.2%	0.2%	-0.0%
	σ_z	$\{\frac{1}{2}, \frac{1}{2}\}$	-.0757	7.1%	5.5%	0.5%	0.8%	.4784	-0.1%	0.2%	0.1%	0.0%
		$\{\frac{1}{2}, -\frac{1}{2}\}$.0131	2.3%	1.1%	0.0%	-0.1%	.0006	79.9%	-0.4%	5.5%	-1.0%

Table 2: Convergence of the one-body matrix elements as in table 1, but at $\omega = 120 \text{ MeV}, \theta = 165^\circ$, where off-diagonal matrix elements $M' \neq M$ are probed more strongly.

Insertions of the proton's or neutron's unit operators produce, of course, the matrix elements with the largest magnitudes, of order 1. For the small momentum transfer at ($\omega = 50 \text{ MeV}, \theta = 30^\circ$), these matrix elements deviate only a little from the zero-energy normalisation of eq. (2.17). At the highest momentum transfer, ($\omega = 120 \text{ MeV}, \theta = 165^\circ$), their values have dropped, as it happens to about a factor of one-half. Similarly large are the neutron's spin-operators $\sigma_x^{(n)}$ and $\sigma_y^{(n)}$ for ($M' = \frac{1}{2}, M = -\frac{1}{2}$), and $\sigma_z^{(n)}$ for ($M' = \frac{1}{2}, M = \frac{1}{2}$). This is well-explained by a naïve model of ^3He as two protons paired to total spin zero, plus a neutron which therefore carries all the ^3He spin. This class of matrix elements is converged in j_{12} to $\lesssim 0.2\%$. It shows little dependence on the potential, typically $\lesssim 2\%$ for ($\omega = 50 \text{ MeV}, \theta = 30^\circ$) and $\lesssim 4\%$ at the higher momentum transfer, ($\omega = 120 \text{ MeV}, \theta = 165^\circ$).

A second class consists of those matrix elements which are suppressed by factors of 10 to 100: insertions of the proton's spin-operators $\sigma_z^{(p)}$ and $\sigma_x^{(p)}$ for any combination (M', M), or of $\sigma_y^{(p)}$ for ($M' = \frac{1}{2}, M = -\frac{1}{2}$). For each potential separately, they are converged to better than 3%. The difference between results for the two potentials can be as large as 30%, but we note that this translates to only $\lesssim 0.5\%$ relative to the magnitude of the largest matrix elements as defined in eq. (3.9). Not surprisingly, this is a signal that these matrix elements are more sensitive to short-range details of the two- and three-nucleon interactions. In the naïve ^3He model of paired proton-spins and only s -wave interactions, they are zero. For realistic interactions, they are nonzero because of the small d -wave and s' -wave contributions in which the proton spins are parallel. Most modern potentials yield a d -wave "probability" of $\lesssim 10\%$ in ^3He , and while this is of course not an observable, it is

instructive as an indicator of how complex a potential is to solve numerically. AV18+UIX, with its hard core and correspondingly higher amount of two-body sd -mixing creates larger matrix elements which also converge more slowly.

All the other matrix elements are $\lesssim 10^{-3}$ and thus usually irrelevant for observables. With differences of $\lesssim 10\%$ between potentials, they are again more sensitive to short-distance details. But they are converged for each individual potential to between $\lesssim 1\%$ and $\lesssim 0.001\%$ relative to the magnitude of the largest matrix elements, *cf.* (3.9).

We take convergence in j_{12} as a sign of numerical stability, and differences between potentials as signs of some residual theoretical uncertainties associated with short-distance pieces of the Compton response that are of higher order in χ EFT. Therefore, we find that relative to the magnitude of the largest one-body matrix elements defined in eq. (3.9), the numerical error never exceeds 0.2%. Theoretical uncertainties due to potential choice are less than 2% at the smaller momentum transfer, or 4% at the larger one. There are, of course, other theoretical uncertainties induced by the truncation of the χ EFT Compton kernels. Now, we are not concerned with those, but refer to their assessment in ref. [28].

3.3.2 Convergence of Two-Body Matrix Elements

Turning now to the results for two-body densities, we consider the matrix elements when the two-body kernel coupling the two Compton photons to the charged exchange-pion is inserted; see sect. 3.1.3. We use a sequence $j_{12} \leq 1, 2, 3, 4$ to study convergence. Like for the one-body-densities, production times for two-body densities should roughly increase with the square of the number of channels, but they must be produced for a sufficiently fine grid of momenta (p'_{12}, p_{12}). Actual runtimes scale somewhat better for small j_{12} , indicating that preparations are relatively less time-consuming. Compared to the production time for a density with $j_{12} \leq 1$, one with $j_{12} \lesssim 2$ takes about 2.4 times as long, compared to a factor 4 from the rough estimate; 6 times for $j_{12} \lesssim 3$ (estimate: 7 times); 16 times for $j_{12} \lesssim 4$ (estimate: 14 times); and 29 times for $j_{12} \lesssim 5$ (estimate: 20 times). Computing a two-body density with $j_{12} \leq 5$ takes about fifteen times longer than the corresponding one-body density, namely about 35 s on JURECA, using 8 nodes with 68 cores each, or less than 6 CPU-hours. In order to go from densities to matrix elements, one must perform the radial and angular integrations over \vec{p}_{12} and summation over quantum numbers in the (12) subsystem, see eq. (2.21). On a workstation, that adds less than half an hour per energy and angle for $j_{12} \leq 1$, a few hours or a factor of ≈ 8 for $j_{12} \leq 2$, a workday or another factor of ≈ 3 for $j_{12} \leq 3$, a full day or another factor of ≈ 3 for $j_{12} \leq 4$, and two full days or another factor of 2 for $j_{12} \leq 5$. One could expedite this by multipole-expanding the kernel, but the same computations in the “traditional” approach take many times that; see sect. 3.4.2.

As we did for the one-body densities, we discuss the extent to which the normalisation of eq. (2.23) is fulfilled. We confirmed that for densities at zero momentum-transfer and $j_{12} \leq 4$, the relative difference is $\lesssim 5.2 \times 10^{-3}$. Individually, the operator of eq. (2.26) undercounts both the number of proton and neutron pairs by about the same 0.5%, each. In either case, a relative accuracy of $< 6.6 \times 10^{-3}$ for the normalisation of the two-body density is already achieved for $j_{12} \leq 2$.

$$\omega = 50 \text{ MeV}, \theta = 30^\circ$$

$\{M', M; \lambda', \lambda\}$	Idaho N ³ LO+3NFb			AV18+UIX				
	value [fm ³]	$1 - \frac{j_{12} \leq 1}{j_{12} \leq 4}$	$1 - \frac{j_{12} \leq 2}{j_{12} \leq 4}$	$1 - \frac{j_{12} \leq 3}{j_{12} \leq 4}$	value [fm ³]	$1 - \frac{j_{12} \leq 1}{j_{12} \leq 4}$	$1 - \frac{j_{12} \leq 2}{j_{12} \leq 4}$	$1 - \frac{j_{12} \leq 3}{j_{12} \leq 4}$
$\{\frac{1}{2}, \frac{1}{2}; 1, 1\}$	-.07139	0.65%	0.10%	0.03%	-.09394	1.15%	0.54%	0.06%
$\{\frac{1}{2}, \frac{1}{2}; -1, 1\}$	-.00543	0.68%	0.11%	0.03%	-.00706	1.15%	0.55%	0.07%
$\{\frac{1}{2}, \frac{1}{2}; 1, -1\}$	-.00543	0.68%	0.11%	0.03%	-.00706	1.15%	0.55%	0.07%
$\{\frac{1}{2}, \frac{1}{2}; -1, -1\}$	-.07139	0.65%	0.10%	0.03%	-.09394	1.15%	0.54%	0.06%

Table 3: Convergence of the two-body matrix elements for the meson-exchange kernel of ³He Compton scattering with photon helicities (λ', λ) for potentials Idaho N³LO+3NFb and AV18+UIX in the “density” approach with $j_{12} \leq 1$ up to $j_{12} \leq 4$ at $\omega = 50 \text{ MeV}, \theta = 30^\circ$, where mostly diagonal matrix elements are probed. The value for $j_{12} \leq 4$ is in fm³ and normalised as in eq. (2.23). Matrix elements with $M' \neq M$ are not shown as they have magnitudes $< 2 \times 10^{-7} \text{ fm}^3$ and are hugely sensitive to numerical noise but do not bear on any observable. Matrix elements with $M' = -\frac{1}{2}$ follow from those quoted by time-reversal invariance, see eq. (2.31). See text and caption to table 1 for further details.

Tables 3 and 4 show convergence patterns and converged matrix elements for $M' = \frac{1}{2}$, normalised following eq. (2.23) and quoted in fm³. Matrix elements with $M' = -\frac{1}{2}$ follow again from time-reversal invariance (see app. B), with eqs. (2.28) and (2.30) translating to:

$$A_{-M, -\lambda}^{-M', -\lambda'} = (-1)^{M' - M + \lambda' - \lambda} A_{M, \lambda}^{M', \lambda'} . \quad (3.12)$$

Matrix elements with $M' \neq M$ are not displayed since they have magnitudes $< 2 \times 10^{-7} \text{ fm}^3$, *i.e.* are smaller than those with $M' = M$ by a factor of $< 10^{-4}$. They have no impact on observables but are quite susceptible to numerical noise. The pair of matrix elements with $(\lambda = \lambda')$ appear to be identical in the table, as do those with $(\lambda = -\lambda')$. Closer inspection reveals small relative differences of magnitude $\leq 10^{-6}$, attributed to numerical noise.

There is clear convergence: even the $j_{12} \leq 1$ answers make up $> 98.6\%$ of those with $j_{12} \leq 4$. The progression is monotonic for all quantum numbers and kinematic points. There are no stark differences between small and large momentum-transfers. With $j_{12} \leq 4$, all matrix elements are known to $\lesssim 0.1\%$, which is far better than for the one-body elements. There also appears to be much more sensitivity to short-range details, as the differences between answers using AV18+UIX or the chiral Idaho potential are of the order of 25%, again at all energies, angles and quantum numbers. This sensitivity of two-body matrix elements to the NN potential—and in particular to the amount of *sd*-mixing—was already observed for the deuteron [48]. Ref. [47] showed that including rescattering effects completely removes the potential dependence as $\omega \rightarrow 0$, since it restores the Thomson limit. The dependence on the NN potential is then also much reduced at $\omega \approx 100 \text{ MeV}$: to only about 0.5% in the cross section, with similar reductions in other observables [49].

$$\omega = 120 \text{ MeV}, \theta = 165^\circ$$

$\{M', M; \lambda', \lambda\}$	Idaho N ³ LO+3NFb			AV18+UIX				
	value [fm ³]	$1 - \frac{j_{12} \leq 1}{j_{12} \leq 4}$	$1 - \frac{j_{12} \leq 2}{j_{12} \leq 4}$	$1 - \frac{j_{12} \leq 3}{j_{12} \leq 4}$	value [fm ³]	$1 - \frac{j_{12} \leq 1}{j_{12} \leq 4}$	$1 - \frac{j_{12} \leq 2}{j_{12} \leq 4}$	$1 - \frac{j_{12} \leq 3}{j_{12} \leq 4}$
$\{\frac{1}{2}, \frac{1}{2}; 1, 1\}$	-.00149	0.72%	0.13%	0.03%	-.00190	1.33%	0.73%	0.06%
$\{\frac{1}{2}, \frac{1}{2}; -1, 1\}$	-.10240	0.87%	0.19%	0.05%	-.12658	1.33%	0.70%	0.11%
$\{\frac{1}{2}, \frac{1}{2}; 1, -1\}$	-.10240	0.87%	0.19%	0.05%	-.12658	1.33%	0.70%	0.11%
$\{\frac{1}{2}, \frac{1}{2}; -1, -1\}$	-.00149	0.72%	0.13%	0.03%	-.00190	1.33%	0.73%	0.06%

Table 4: Convergence of the two-body matrix elements as in table 3, but at $\omega = 120 \text{ MeV}, \theta = 165^\circ$, where off-diagonal matrix elements are probed more strongly. See also text and captions to tables 1 and 3 for further details.

3.4 Comparison of the Two Approaches

The “traditional” and density approaches encode the same Physics. One might thus expect that they lead to identical results. However, even if both calculations were perfectly converged individually, we would not expect perfect agreement with previous publications. The main reasons for remaining discrepancies are somewhat subtle:

- (1) Due to a decade and a half of advances in computing power, the wave functions used in the densities approach have finer momentum-spaced grids and correspondingly smaller interpolation errors.
- (2) The “traditional” code’s wave functions were obtained from Faddeev calculations in momentum space [50, 51] in a parametrisation that has since been superseded.
- (3) There are small differences in the NN and 3N potentials between the code which produced the traditional wave functions 15 years ago and the new implementation to construct the densities. This includes slightly different numerical values for the two-pion and three-nucleon interactions.
- (4) In the traditional approach, the struck nucleon in the one-body code was the one labelled as “1” (the “innermost”), not “3” (the “outermost”). Therefore, truncation at a fixed j_{12} does not mean the same thing in the two approaches.

We do not expect any of these issues to affect the results by more than 1%. In previous publications, the goal was to achieve a numerical accuracy which was better than the thickness of the lines in plots of observables, and considerably smaller than the overall accuracy of roughly $\lesssim 3\%$ of the χ EFT expansion; see detailed discussion in ref. [28, sect. 2.4.3]. Physics, rather than numerics, was the focus, and including ³He channels up to $j_{12} = 2$ achieved the goal. Now, we compare instead our new approach to Compton scattering with those previous $j_{12}^{\text{max}} = 2$ results. The points of difference listed above could, in principle,

$$\omega = 50 \text{ MeV}, \theta = 30^\circ$$

insertion		Idaho N ³ LO+3NFb				AV18+UIX			
		proton		neutron		proton		neutron	
σ_μ	$\{M', M\}$	value	rel.dev.	value	rel.dev.	value	rel.dev.	value	rel.dev.
σ_0	$\{\frac{1}{2}, \frac{1}{2}\}$	1.9678	-0.12%	.9861	-0.03%	1.9560	0.15%	.9791	0.08%
σ_x	$\{\frac{1}{2}, -\frac{1}{2}\}$	-.0398	0.07%	.8809	0.54%	-.0496	3.70%	.8610	0.76%
$i\sigma_y$	$\{\frac{1}{2}, -\frac{1}{2}\}$	-.0376	0.23%	.8810	0.55%	-.0476	3.91%	.8611	0.76%
σ_z	$\{\frac{1}{2}, \frac{1}{2}\}$	-.0378	0.22%	.8810	0.55%	-.0478	3.90%	.8611	0.76%
	$\{\frac{1}{2}, -\frac{1}{2}\}$.0006	-2.63%	.0000	8.37%	.0005	-1.09%	.0000	5.99%

Table 5: Comparison of the independent nonzero one-body matrix elements in ^3He with insertions $3\sigma_\mu^{(N)}$ for the proton and neutron, for potentials Idaho N³LO+3NFb and AV18+UIX. The column “rel. dev.” denotes the relative difference, as defined in eq. (3.8), between the “density” and “traditional” approach with $j_{12} \leq 2$ at $\omega = 50 \text{ MeV}, \theta = 30^\circ$, where mostly diagonal matrix elements are probed. See text and caption to table 1 for further details.

be improved in the traditional code. But we have decided to “retire” that inefficient implementation after verifying that the densities approach reproduces it to acceptable accuracy. Thus, our standard for agreement between the two approaches is 1%.

Finally, we note that comparing the one-body insertions $\sigma_\mu^{(N)}$ with $j_{12} = 2, 3$ in the two approaches helped us diagnose a mistake in the implementation of the “traditional approach” which is discussed in app. A. There was a noticeable disagreement between the two approaches, until that was corrected.

3.4.1 Comparison of One-Body Matrix Elements

In ref. [28], we studied numerical convergence only of the overall Compton one-body matrix elements. These are dominated by γN interactions which do not involve nucleon-structure effects such as the nucleon polarisabilities, *e.g.* the Thomson term (insertion of $\sigma_0^{(N)} \equiv \mathbb{1}$) as well as the minimal electric and magnetic-moment couplings to the nucleon. Therefore, including all partial waves with $j_{12} \leq 2$ in the “traditional” one-body matrix elements sufficed for convergence of Compton matrix elements to within 0.5% at the highest energy and momentum-transfer we considered. The cross section was then numerically converged at about 1.2% or 0.35 nb/sr there, and considerably better elsewhere.

In contradistinction, we now compare the ^3He matrix elements at a given energy and angle for each of the 8 insertions $\sigma_\mu^{(N)}$, *i.e.* we look at more than just overall one-body Compton matrix elements. We reiterate that in what follows, we do not compare to the “fully converged” density results with $j_{12} \leq 5$ of sect. 3.3.1, but to those which use the same $j_{12} \leq 2$ as the “traditional” approach.

Tables 5 and 6 show that the two methods agree very well. The matrix elements of order

$$\omega = 120 \text{ MeV}, \theta = 165^\circ$$

insertion		Idaho N ³ LO+3NFb				AV18+UIX			
		proton		neutron		proton		neutron	
σ_μ	$\{M', M\}$	value	rel.dev.	value	rel.dev.	value	rel.dev.	value	rel.dev.
σ_0	$\{\frac{1}{2}, \frac{1}{2}\}$.9913	-0.06%	.5424	0.76%	1.0230	-0.43%	.5622	1.13%
σ_x	$\{\frac{1}{2}, -\frac{1}{2}\}$.0385	5.16%	.4793	0.98%	.0251	2.58%	.4822	1.33%
$i\sigma_y$	$\{\frac{1}{2}, -\frac{1}{2}\}$.0404	4.92%	.4794	0.98%	.0269	2.46%	.4823	1.33%
σ_z	$\{\frac{1}{2}, \frac{1}{2}\}$	-.0683	-2.89%	.4740	0.97%	-.0715	-0.08%	.4777	1.30%
	$\{\frac{1}{2}, -\frac{1}{2}\}$.0143	0.01%	.0007	1.73%	.0130	0.61%	.0006	4.54%

Table 6: Comparison of the one-body matrix elements as in table 5, but at $\omega = 120 \text{ MeV}, \theta = 165^\circ$, where off-diagonal matrix elements are probed more strongly.

1 agree to $\approx 1\%$ and better. Those of order $10^{-[1\dots 2]}$ show somewhat more variance, with a relative deviation as defined in eq. (3.8) of $\lesssim 5\%$ at the largest momentum transfers. That is still less than 0.5% of the spin-helicity contributions with the largest magnitudes at a given energy and angle; see criterion in eq. (3.9). Matrix elements with magnitudes of order 10^{-4} and smaller show up to 8% relative variation, or $\lesssim 0.01\%$ relative to the matrix element with the largest magnitude. The agreement is usually better for the chiral potential than for AV18+UIX, as its harder core needs a finer interpolation in densities and wave functions.

3.4.2 Comparison of Two-Body Matrix Elements

In the “traditional” two-body matrix elements, a maximum total angular momentum of the (12) subsystem $j_{12} \leq 1$ provides a reasonable compromise between runtime and numerical accuracy. With an increase to $j_{12} \leq 2$, the matrix elements change by barely more than 0.7% for either choice of potential—even at the highest energies and momentum transfers considered. However, the runtime increases nearly tenfold, from CPU-hours to days per energy and angle, and even then their numerical accuracy is not quite as good as that of the density method; see the enumeration at the beginning of sect. 3.4. Certainly then, going to $j_{12} = 3$ is not worthwhile for the two-body matrix elements we consider here. Therefore, we decided to compare results for $j_{12} \leq 2$.

Only matrix elements which are negligible (namely $< 10^{-6}$ relative to the biggest ones) show substantial relative differences upon the inclusion of channels with $j_{12} = 2$. All this is consistent with the pattern which emerged in the convergence-check of the density results as well; see sect. 3.3.2.

Bearing in mind that the numerical treatment of the (12) subsystem is identical and indeed uses the same code, it is not surprising that the CPU-time for two-body matrix elements increases roughly by a factor of 10 from $j_{12} \leq 1$ to ≤ 2 in both the “traditional” and density approach. But the “traditional” matrix-element evaluation is about 20 times

	$\omega = 50 \text{ MeV}, \theta = 30^\circ$				$\omega = 120 \text{ MeV}, \theta = 165^\circ$			
	Idaho N ³ LO+3NFb		AV18+UIX		Idaho N ³ LO+3NFb		AV18+UIX	
$\{M', M; \lambda', \lambda\}$	value [fm ³]	rel.dev.	value [fm ³]	rel.dev.	value [fm ³]	rel.dev.	value [fm ³]	rel.dev.
$\{\frac{1}{2}, \frac{1}{2}; 1, 1\}$	-.07132	0.1%	-.09343	0.2%	-.00149	0.0%	-.00188	0.2%
$\{\frac{1}{2}, \frac{1}{2}; -1, 1\}$	-.00543	0.3%	-.00702	0.3%	-.10220	0.8%	-.12570	0.8%
$\{\frac{1}{2}, \frac{1}{2}; 1, -1\}$	-.00543	0.3%	-.00702	0.3%	-.10220	0.8%	-.12570	0.8%
$\{\frac{1}{2}, \frac{1}{2}; -1, -1\}$	-.07132	0.1%	-.09343	0.2%	-.00149	0.0%	-.00188	0.2%

Table 7: Comparison of two-body matrix elements in the “density” approach and the “traditional” approach for potentials Idaho N³LO+3NFb and AV18+UIX with $j_{12} \leq 2$ at $\omega = 50 \text{ MeV}, \theta = 30^\circ$ (where mostly diagonal matrix elements are probed) and $\omega = 120 \text{ MeV}, \theta = 165^\circ$ (where off-diagonal matrix elements are probed more strongly). See also text and captions to tables 5 and 3 for further details.

slower in each case. It spends the vast majority of its time on the part which is encoded in the two-body densities that serve as input in the “densities” approach. A minor price to pay is that the two-body densities are very big; see the end of sect. 2.4.

As can be seen in table 7, “traditional” and density approach agree to better than 0.3% for the chiral potential, and better than 1% for AV18+UIX even at the higher energies and momentum transfers, based on the criterion of eq. (3.8). That is very close to the difference between the results at $j_{12} \leq 2$ and the converged result; *cf.* tables 3 and 4.

We therefore conclude that the one- and two-body matrix elements agree very well in the two approaches—namely to within the 1% expected after the discussion of difference between the two implementations in the opening of sect. 3.4.

4 Summary and Outlook

We introduced a transition-density method that employs pre-computed one- and two-body densities in the evaluation of elastic processes in which momentum is transferred to an A-nucleon system, and used Compton scattering on ³He as a test case. Extensions to charge-transfer or inelastic processes, to incorporate few-body transition densities with $n \geq 3$ nucleons active in the reaction process and to other targets are conceptually relatively straightforward.

The method has several attractive features. Producing transition densities is the computationally most demanding aspect of the method—but once produced, they can be applied to a host of reactions. Therefore, their quality for a particular nucleus can be extensively benchmarked against known processes, and computational resources and development can be focused on densities. On the other hand, a particular reaction kernel involves only those nucleons which interact with the probe, and not the spectators. Therefore, the quality of a kernel can be benchmarked across different nuclei. Once the pertinent one- and few-body

densities have been calculated for a new nucleus, only small changes in existing matrix-element calculations are required, *e.g.* because of the different quantum numbers of the particular nuclear ground states. The computational effort needed to go from a given kernel and a given set of densities to interaction matrix elements is therefore hardly different for an arbitrary nucleus than it is for, say, ${}^3\text{He}$.

In our example of coherent Compton scattering, the single- and two-nucleon Compton kernel are already available in the one- and two-nucleon Hilbert spaces, respectively. The improvement achieved here therefore opens the way to using the same operators for Compton matrix elements on other nuclei with $A \geq 3$, like ${}^4\text{He}$. Once we have densities for heavier targets, Compton matrix elements can be produced quickly.

In Compton scattering on ${}^3\text{He}$, the densities-based method also turned out to be markedly faster than the calculational strategy employed previously. This allowed for detailed convergence studies with an unprecedented number of partial waves. These show very good numerical convergence even for a comparatively hard underlying potential like AV18 with the Urbana-IX 3N interaction. Such investigations would have been prohibitively expensive in the previously-used method. The new method produces results which agree with the traditional ones at the expected level for both a “hard” and “soft” NN and 3N interaction, taking into account the limitations of the calculational aspects of the old implementation. Having such similar results from two largely different codes and methodological approaches makes us confident that the coding and numerics is fully understood.

It was not our goal here to provide predictions that can be compared with data. Instead, we wanted to validate our new, computationally less intensive, densities-based method. Nevertheless, it is useful to provide some context—and perhaps inject some caution—regarding the numbers presented above. We thus recapitulate part of the discussion of ref. [28] here. For our high-energy results at $\omega \approx 120$ MeV, the kernel and ${}^3\text{He}$ state are complete up to and including chiral order $e^2\delta^3$, where $\delta \approx 0.4$ is the typical size of the expansion parameter [38, 40]. The first omitted terms can thus be estimated as $\mathcal{O}(e^2\delta^4) \lesssim 3\%$ in the amplitudes, or twice that in a cross section. These omitted terms include “rescattering” as discussed in the Introduction and sect. 2.1: the coherent propagation of all target nucleons between photon absorption and emission. As $\omega \rightarrow 0$, however, rescattering becomes dominant and the chiral power counting changes [6, 52].

As the photon energy decreases, the importance of rescattering increases gradually. In the deuteron, rescattering accounts indeed for about 3% of the cross section at $\omega \approx 90$ MeV, in line with the analysis of the previous paragraph, but it is a 20% effect at $\omega \approx 45$ MeV (see fig. 5.3 of ref. [6]). This is consistent with its effect scaling as $1/(\omega - \omega_{\text{coll}})$, where ω_{coll} is the scale at which resummation becomes unavoidable. We suspect $\omega_{\text{coll}} \sim m_\pi^2/M_N$ with M_N the nucleon mass, since m_π is the typical momentum scale of the interaction [38, 47]. This scale would then not be especially nucleus dependent—albeit we expect it is somewhat higher in ${}^3\text{He}$ than in the deuteron. This suggests that the results presented above have a theoretical uncertainty of about 20% at $\omega \approx 50$ MeV. While this is clearly insufficient for high-accuracy comparisons with data, even a 20% uncertainty can suffice to encourage and guide experimental planning and data taking. A more reliable quantification of the uncertainty from rescattering needs a computation of coherent- A -body rescattering in ${}^3\text{He}$.

This is under way [53].

Another obvious next step is the calculation of densities for ${}^4\text{He}$ and of its elastic Compton cross section at energies up to about 120 MeV. Those can then be compared with the recent data from HI γ S [30, 31] with the goal of extracting high-accuracy values for the nucleon polarisabilities. As the two-nucleon operators considered here are quite similar to those for dark-matter scattering on nuclei, we also intend to use previous dark-matter- ${}^4\text{He}$ scattering calculations [11, 54] as benchmarks for an evaluation with pre-computed densities.

Targets beyond ${}^4\text{He}$ are, again, not computationally more costly, once densities have been computed. Compton scattering off heavier targets, like ${}^6\text{Li}$ [29], will presumably require densities from No-Core Shell Model wave functions [55]. In this regard, the approach adopted here has much in common with the recent work of Burrows *et al.*, where single-body densities were used to compute nucleon-nucleus optical potentials for ${}^4\text{He}$, ${}^6\text{He}$, ${}^{12}\text{C}$ and ${}^{16}\text{O}$ [17–19]. In that case, however, a different, non-local, density enters, since the density is folded with the nucleon-nucleon T -matrix, and not with an operator that is local in coordinate space. Two-body densities were not considered in ref. [17], either; they would presumably be required in a calculation of 3N-interaction corrections to the optical potential.

So far, we produced only densities for one-body operators which depend at most linearly on the total cm momentum of the nucleus, besides the dependence on the momentum-transfer. For now, the two-body densities require two-body operators that are independent of the total momentum of the nucleus. The extension to higher-rank dependence on the momentum of the nucleus is straightforward if needed.

The transition-density method has applications well beyond Compton scattering; a cornucopia of processes can be computed with the densities introduced here. Any elastic scattering process in which a probe interacts perturbatively with ${}^3\text{He}$ can be evaluated using our densities, provided the pertinent reaction kernels are written as momentum-space interactions with only one or two active nucleons, and as long as they fulfil the criteria stated in the previous paragraph. For example, the one-body densities are exactly those needed to compute single-nucleon operator contributions to electron scattering on a nucleus. Likewise, the two-body densities are sufficiently general that they can be used to compute exchange-current corrections to the form factors from two-body operators in momentum space.

Practitioners interested in convoluting momentum-space operators with our ${}^3\text{He}$ densities can find them at <https://datapub.fz-juelich.de/anogga>. Densities are provided for AV18 with Urbana-IX 3N [20, 21] interaction and the chiral Idaho N³LO potential at cutoff 500 MeV [22] with the “ $\mathcal{O}(Q^3)$ ” χ EFT 3N interaction of variant “b” of ref. [23]. We will provide densities based on other modern, sophisticated potentials in the future and encourage practitioners to contact us with requests for further extensions.

Acknowledgements

We thank Mike Birse for useful input at a couple of stages of this work. DRP thanks Charlotte Elster and Matt Burrows for informative discussions. The stimulating environment

and financial support of the INT in Seattle came at a critical juncture of this research. We are therefore grateful to the organisers and participants of the INT “Programme 18-2a: Fundamental Physics with Electroweak Probes of Light Nuclei” and INT workshop “From Nucleons to Nuclei: Enabling Discovery for Neutrinos, Dark Matter And More”. HWG acknowledges the warm hospitality and financial support of Ohio University, the University of Manchester and Forschungszentrum Jülich which was instrumental for this research. Likewise, AN is grateful for the warm hospitality and financial support of Ohio University. DRP is grateful for the warm hospitality of the IKP Theoriezentrum, Darmstadt. This work was supported in part by the US Department of Energy under contract DE-SC0015393 (HWG) and DE-FG02-93ER-40756 (DRP), by the UK Science and Technology Facilities Council grant ST/P004423/1 (JMcG), by the ExtreMe Matter Institute EMMI at the GSI Helmholtzzentrum für Schwerionenphysik, Darmstadt, Germany (DRP), and by the Deutsche Forschungsgemeinschaft and the Chinese National Natural Science Foundation through funds provided to the Sino-German CRC 110 “Symmetries and the Emergence of Structure in QCD” (AN; DFG grant no. TRR 110; NSFC grant no. 11621131001). Additional funds for HWG were provided by an award of the High Intensity Gamma-Ray Source HI γ S of the Triangle Universities Nuclear Laboratory TUNL in concert with the Department of Physics of Duke University, and by George Washington University: by the Office of the Vice President for Research and the Dean of the Columbian College of Arts and Sciences; by an Enhanced Faculty Travel Award of the Columbian College of Arts and Sciences. His research was conducted in part in GW’s Campus in the Closet. The computations of nuclear densities were performed on JURECA and the JURECA-BOOSTER of the Jülich Supercomputing Centre (Jülich, Germany).

A Comment on Prior Compton Calculations on ${}^3\text{He}$

Our previous strategy for the computation of ${}^3\text{He}$ matrix elements of the Compton operators was based on the photodissociation calculation of ref. [56]. The analogous integrals for one-body and two-body operator contributions to the matrix elements were performed without splitting them into reaction-mechanism and density parts. While they were factorised into a piece involving the nucleons taking part in the reaction and the matrix element of the spectator δ -distribution, the efficiency of defining densities that refer only to the quantum numbers of the active nucleons was not noticed; see refs. [24–28] for details.

In the course of this study, we found that refs. [24–28] contain a flaw in the reasoning leading to the original equations corresponding to eq. (3.1), which in turn led to incorrect numerical implementations of the one-body part. The struck nucleon in the one-body part was considered to be not nucleon 3 but one of the nucleons of the (12) sub-system. Therefore, rather than $\hat{O}_{\lambda\lambda}^{1B}(3)$ as in sect. 2.3, the operator $\hat{O}_{\lambda\lambda}^{1B}(1)$ was considered and replaced by $\frac{1}{2}[\hat{O}_{\lambda\lambda}^{1B}(1) + \hat{O}_{\lambda\lambda}^{1B}(2)]$ in the course of defining operators on the space of two-nucleon states. However, this replacement cannot be done at the level of the spin and isospin operators because the momentum assignment for the post-collision state differs depending on whether the struck particle is nucleon 1 or nucleon 2.

That error in refs. [24–27] was also present in our recent evaluation of $\gamma^3\text{He}$ scattering [28]. It means that those works missed contributions at nonzero momentum-transfer, where the Compton-scattering collision induced a transition that changed either the spin or the isospin of the NN state, but not both.

Fortunately, the numerical effect on observables is very small. For the neutron, this changes the matrix elements with insertions of $3\sigma_\mu$ by $\leq 3\%$, except for about 16% in σ_x at the highest energy and momentum transfer we consider ($\omega = 120$ MeV, $\theta = 165^\circ$). The change is more pronounced for the proton, where it can amount to a factor of about 4.5 in σ_x at that point and exceeds 10% even at small (ω, θ) . This might seem to imply big changes of the one-body amplitudes for the spin-polarisabilities. But the proton spins inside ${}^3\text{He}$ are mostly paired to spin-zero, so there is hardly any sensitivity to the mistake in matrix elements of the proton spin. The effect is also shielded for the neutron spin. Even at the “high” energy and momentum-transfer tested here, the effect of the neutron’s spin-polarisabilities is $\approx 10\%$ in the amplitude. Matrix elements of the neutron’s spin do not play a big role, and even a 16% error in them would only be a 1.6% error in matrix elements. This is associated with the fact that the biggest contributions to ${}^3\text{He}$ Compton scattering for 50 MeV $\lesssim \omega \lesssim 120$ MeV come from interactions with the two charged protons. These do not change the nucleon spin and are hence proportional to insertions of $\mathbb{1} \equiv \sigma_0$ —and such matrix elements are changed by less than 0.2% of the largest magnitude of all one-body matrix elements, see eq. (3.9). Therefore, we were able to find the error only when we zoomed in on a detailed comparison between the “traditional” and “density” approach; see sect. 3.4. In the “traditional” results quoted in the body of the paper this error is, of course, corrected.

In almost all cases, this mistake for the matrix elements with insertions $\sigma_\mu^{(N)}$ only minimally alters the plots of both magnitudes and sensitivities of observables in ref. [28]. The

cross section as well as the double-asymmetries $T_{11}^{\text{circ}} \equiv \Sigma_{2x}$ and $T_{10}^{\text{circ}} \equiv \Sigma_{2z}$ change by $< 1\%$ at 50 MeV, and by $\lesssim 3\%$ at 120 MeV, where asymmetries exceed 0.1. For $\Sigma^{\text{lim}} \equiv \Sigma_{30}$, the thickness of the line is never exceeded ($< 1\%$). To put this into perspective, the variation from using different ${}^3\text{He}$ wave functions is at all energies and angles at least a factor five bigger than the change from this error. In ref. [28], wave-function dependence was, in turn, estimated to be substantially smaller than the sum of all residual theoretical uncertainties. Therefore, we refrain from amending or updating the presentations of refs. [25–28]. Their conclusions are unchanged.

B Symmetries of Matrix Elements

We now derive the symmetries that relate different matrix elements of the one- and two-nucleon operators in sects. 3.4 and 3.3 by considering an insertion $\sigma_\mu e^{i\frac{2}{3}\vec{q}\cdot\vec{r}_3}$, which is independent of \vec{k} (*i.e.* $K = \kappa = 0$). Note that we have employed the Jacobi-coordinate-space representation of the momentum-conservation relation (2.12) here to define the operator insertion. Hence, the plane wave deposits momentum into the Jacobi co-ordinate of nucleon 3. Also, $\sigma_\mu^{(N)}$ acts not on the ${}^3\text{He}$ nucleus as a whole but only on the single “active” nucleon 3 at coordinate \vec{r}_3 . Therefore, this set of operators cannot be represented by the standard Pauli matrices. However, their matrix elements do retain certain properties of a spin- $\frac{1}{2}$ representation.

We first prove relation (3.10). Under time reversal, $\mathcal{T}\sigma_i^{(N)}\mathcal{T}^{-1} = -\sigma_i^{(N)}$ is odd, while $\mathcal{T}\sigma_0^{(N)}\mathcal{T}^{-1} = \sigma_0^{(N)}$ is even. Since we wish to consider only operators with real matrix elements, we also note that $\mathcal{T}i\sigma_y^{(N)}\mathcal{T}^{-1} = i\sigma_y^{(N)}$ is even.

Now denoting the state $\mathcal{T}|\psi\rangle$ by $|\tilde{\psi}\rangle$, time reversal invariance gives for the matrix element of some operator \mathcal{Q} , see *e.g.* ref. [57]:

$$\langle\phi|\mathcal{Q}|\psi\rangle = \langle\tilde{\psi}|\mathcal{T}\mathcal{Q}^\dagger\mathcal{T}^{-1}|\tilde{\phi}\rangle . \quad (\text{B.1})$$

If the matrix element is real, then $\langle\phi|\mathcal{Q}|\psi\rangle = \langle\psi|\mathcal{Q}^\dagger|\phi\rangle$, so

$$\langle\psi|\mathcal{Q}^\dagger|\phi\rangle = \langle\tilde{\psi}|\mathcal{T}\mathcal{Q}^\dagger\mathcal{T}^{-1}|\tilde{\phi}\rangle . \quad (\text{B.2})$$

This, of course, remains true if we replace \mathcal{Q}^\dagger with \mathcal{Q} , which now serves as our starting point. Recalling eq. (2.28)

$$\mathcal{T}|j, m_j\rangle = (-1)^{j+m_j} |j, -m_j\rangle , \quad (\text{B.3})$$

we obtain

$$\langle M'|\sigma_{x,z}^{(N)}|M\rangle = (-1)^{2J+M'+M-1} \langle -M'|\sigma_{x,z}^{(N)}| -M\rangle \quad (\text{B.4})$$

$$\langle M'|\sigma_0^{(N)}|M\rangle = (-1)^{2J+M'+M} \langle -M'|\sigma_0^{(N)}| -M\rangle \quad (\text{B.5})$$

$$\langle M'|i\sigma_y^{(N)}|M\rangle = (-1)^{2J+M'+M} \langle -M'|i\sigma_y^{(N)}| -M\rangle . \quad (\text{B.6})$$

As $2(J + M)$ is even for both half-integer and integer quantum numbers, this proves eq. (3.10). Replacing $\sigma_\mu^{(N)} \rightarrow \sigma_\mu^{(N)} e^{i\frac{2}{3}\vec{q}\cdot\vec{r}_3}$ does not alter this argument since the plane wave is time-reversal even (parity guarantees that only its real parts can contribute to the final result). Accounting for the multipolarity of \vec{k} ($K \neq 0$), the relation is modified to:

$$A_{-M}^{-M'}(\sigma_\mu^{(N)}; K, -\kappa, \vec{q}) = (-1)^{M'-M+\mu+\kappa} A_M^{M'}(\sigma_\mu^{(N)}; K, \kappa, \vec{q}) . \quad (\text{B.7})$$

This proves there are at most eight independent matrix elements of the $\sigma_\mu^{(N)} e^{i\frac{2}{3}\vec{q}\cdot\vec{r}_3}$ operator in the spin- $\frac{1}{2}$ basis ($M'M$). We now discuss symmetries that eliminate three more. First, since $i\sigma_y^{(N)}$ is both real and anti-Hermitian, both its diagonal elements must be zero:

$$A_M^M(i\sigma_y^{(N)}; \vec{q}) \equiv \langle M | i\sigma_y^{(N)} e^{i\frac{2}{3}\vec{q}\cdot\vec{r}_3} | M \rangle = 0 . \quad (\text{B.8})$$

Furthermore $\sigma_0^{(N)}$ is symmetric, but its off-diagonal elements are equal and opposite by (B.5). Hence they must be zero:

$$A_M^{-M}(\sigma_0^{(N)}; \vec{q}) \equiv \langle -M | \sigma_0^{(N)} e^{i\frac{2}{3}\vec{q}\cdot\vec{r}_3} | M \rangle = 0 . \quad (\text{B.9})$$

These relations can also be established from the Lie algebra of the Pauli operators in a two-dimensional representation that is consistent with time reversal and in which $\sigma_x^{(N)}$ and $\sigma_z^{(N)}$ are real. They do not hold for densities which explicitly depend on \vec{k} (*i.e.* $K \neq 0$).

If the spin of the nucleon were always perfectly aligned with the spin of a $J = \frac{1}{2}$ nucleus, then off-diagonal matrix elements of $\sigma_z^{(N)}$ and diagonal matrix elements of $\sigma_x^{(N)}$ would also be zero. These matrix elements pick out densities for “wrong-spin” to “right-spin” transitions (or vice versa). Specifically:

$$\begin{aligned} \langle -\frac{1}{2} | \sigma_z^{(N)} e^{i\frac{2}{3}\vec{q}\cdot\vec{r}_3} | \frac{1}{2} \rangle &= \rho_{+\frac{1}{2}, +\frac{1}{2}}^{00; m_3^t M_T, -\frac{1}{2}, +\frac{1}{2}} - \rho_{-\frac{1}{2}, -\frac{1}{2}}^{00; m_3^t M_T, -\frac{1}{2}, +\frac{1}{2}} , \\ \langle \frac{1}{2} | \sigma_x^{(N)} e^{i\frac{2}{3}\vec{q}\cdot\vec{r}_3} | \frac{1}{2} \rangle &= \rho_{-\frac{1}{2}, +\frac{1}{2}}^{00; m_3^t M_T, +\frac{1}{2}, +\frac{1}{2}} + \rho_{+\frac{1}{2}, -\frac{1}{2}}^{00; m_3^t M_T, +\frac{1}{2}, +\frac{1}{2}} . \end{aligned} \quad (\text{B.10})$$

Time-reversal alone is not enough to guarantee the equality of these two matrix elements. But the flipping symmetry of eq. (2.38) means that the first terms of each line of eq. (B.10) are equal. Using flipping symmetry in conjunction with time-reversal (2.31) shows that the second terms are equal, too. Therefore, the off-diagonal matrix elements of $\sigma_z^{(N)}$ and diagonal ones of $\sigma_x^{(N)}$ are identical:

$$A_M^{-M}(\sigma_z^{(N)}; \vec{q}) \equiv \langle -M | \sigma_z^{(N)} e^{i\frac{2}{3}\vec{q}\cdot\vec{r}_3} | M \rangle = \langle M | \sigma_x^{(N)} e^{i\frac{2}{3}\vec{q}\cdot\vec{r}_3} | M \rangle \equiv A_M^M(\sigma_x^{(N)}; \vec{q}) . \quad (\text{B.11})$$

Ultimately then, there are five non-equal, non-zero ${}^3\text{He}$ matrix elements of the one-body operators $\{\sigma_0^{(N)}, \sigma_x^{(N)}, \sigma_y^{(N)}, \sigma_z^{(N)}\}$, out of a possible 16. This matches the five independent transition densities after time-reversal, Hermiticity, and flipping symmetry have been applied.

The proof of the two-body relation (3.12) proceeds analogously to that of eq. (B.7). Since the Compton two-body operator \hat{O}_{12} is time-reversal even and the matrix element is real below all thresholds, one finds by inserting eqs. (2.28) and (2.30):

$$\begin{aligned} \langle M' | \langle \lambda' | \mathcal{T} \hat{O}_{12} \mathcal{T}^{-1} | \lambda \rangle | M \rangle &= \langle -M' | \langle -\lambda' | \hat{O}_{12} | -\lambda \rangle | -M \rangle \\ &= (-1)^{2J+M'+M+\lambda'+\lambda} \langle M' | \langle \lambda' | \hat{O}_{12} | \lambda \rangle | M \rangle . \end{aligned} \quad (\text{B.12})$$

Equation (3.12) follows directly because $2(J + M + \lambda)$ is even for both half-integer and integer quantum numbers.

References

- [1] J. Golak, R. Skibinski, H. Witala, W. Glockle, A. Nogga and H. Kamada, Phys. Rept. **415**, 89 (2005) [[nucl-th/0505072](#)].
- [2] S. Bacca and S. Pastore, J. Phys. G **41**, no.12, 123002 (2014) [[arXiv:1407.3490](#) [nucl-th]].
- [3] D. R. Phillips, Ann. Rev. Nucl. Part. Sci. **66**, 421-447 (2016).
- [4] R. Schiavilla, A. Baroni, S. Pastore, M. Piarulli, L. Girlanda, A. Kievsky, A. Lovato, L. Marcucci, S. C. Pieper, M. Viviani and R. Wiringa, Phys. Rev. C **99**, no.3, 034005 (2019) [[arXiv:1809.10180](#) [nucl-th]].
- [5] A. Filin, V. Baru, E. Epelbaum, H. Krebs, D. Möller and P. Reinert, Phys. Rev. Lett. **124**, no.8, 082501 (2020) [[arXiv:1911.04877](#) [nucl-th]].
- [6] H. W. Griesshammer, J. A. McGovern, D. R. Phillips and G. Feldman, Prog. Part. Nucl. Phys. **67**, 841 (2012) [[arXiv:1203.6834](#) [nucl-th]].
- [7] A. Baroni, L. Girlanda, A. Kievsky, L. E. Marcucci, R. Schiavilla and M. Viviani, Phys. Rev. C **94**, no. 2, 024003 (2016) Erratum: [Phys. Rev. C **95**, no. 5, 059902 (2017)] [[arXiv:1605.01620](#) [nucl-th]].
- [8] J. Engel and J. Menéndez, Rept. Prog. Phys. **80**, no. 4, 046301 (2017) [[arXiv:1610.06548](#) [nucl-th]].
- [9] S. Pastore, A. Baroni, J. Carlson, S. Gandolfi, S. C. Pieper, R. Schiavilla and R. Wiringa, Phys. Rev. C **97**, no.2, 022501 (2018) [[arXiv:1709.03592](#) [nucl-th]].
- [10] J. Golak, R. Skibiński, K. Topolnicki, H. Witala, A. Grassi, H. Kamada and L. E. Marcucci, Phys. Rev. C **100**, no. 6, 064003 (2019) [[arXiv:1908.08285](#) [nucl-th]].
- [11] C. Körber, A. Nogga and J. de Vries, Phys. Rev. C **96**, no. 3, 035805 (2017) [[arXiv:1704.01150](#) [hep-ph]].

- [12] J. Bsaisou, U. G. Meißner, A. Nogga and A. Wirzba, *Annals Phys.* **359**, 317 (2015) [[arXiv:1412.5471](#) [hep-ph]].
- [13] H.-W. Hammer, S. König and U. van Kolck, *Rev. Mod. Phys.* **92**, 025004 (2020) [[arXiv:1906.12122](#) [nucl-th]].
- [14] E. Epelbaum, H. W. Hammer and U. G. Meißner, *Rev. Mod. Phys.* **81**, 1773 (2009) [[arXiv:0811.1338](#) [nucl-th]].
- [15] R. Machleidt and F. Sammarruca, *Phys. Scripta* **91**, no. 8, 083007 (2016) [[arXiv:1608.05978](#) [nucl-th]].
- [16] E. Epelbaum, H. Krebs and P. Reinert, *Front. in Phys.* **8**, 98 (2020) [[arXiv:1911.11875](#) [nucl-th]].
- [17] M. Burrows, C. Elster, G. Popa, K. D. Launey, A. Nogga and P. Maris, *Phys. Rev. C* **97**, no. 2, 024325 (2018) [[arXiv:1711.07080](#) [nucl-th]].
- [18] M. Burrows, C. Elster, S. P. Weppner, K. D. Launey, P. Maris, A. Nogga and G. Popa, *Phys. Rev. C* **99**, no. 4, 044603 (2019) [[arXiv:1810.06442](#) [nucl-th]].
- [19] M. Burrows, R. B. Baker, C. Elster, S. P. Weppner, K. D. Launey, P. Maris and G. Popa, *Phys. Rev. C* **102**, no. 3, 034606 (2020) [[arXiv:2005.00111](#) [nucl-th]].
- [20] R. B. Wiringa, V. G. J. Stoks and R. Schiavilla, *Phys. Rev. C* **51**, 38 (1995) [[nucl-th/9408016](#)].
- [21] B. S. Pudliner, V. R. Pandharipande, J. Carlson and R. B. Wiringa, *Phys. Rev. Lett.* **74**, 4396 (1995) [[nucl-th/9502031](#)].
- [22] D. R. Entem and R. Machleidt, *Phys. Rev. C* **68**, 041001 (2003) [[nucl-th/0304018](#)].
- [23] A. Nogga, P. Navratil, B. R. Barrett and J. P. Vary, *Phys. Rev. C* **73**, 064002 (2006) [[nucl-th/0511082](#)].
- [24] D. Choudhury, *PhD thesis*, Ohio University (2006) http://rave.ohiolink.edu/etdc/view?acc_num=ohiou1163711618.
- [25] D. Choudhury, A. Nogga and D. R. Phillips, *Phys. Rev. Lett.* **98** (2007) 232303 [[nucl-th/0701078](#)].
- [26] D. Choudhury, A. Nogga and D. R. Phillips, *Phys. Rev. Lett.* **98**, 232303 (2007) Erratum: [*Phys. Rev. Lett.* **120**, no. 24, 249901 (2018)] [[arXiv:1804.01206](#) [nucl-th]], [[nucl-th/0701078](#)].
- [27] D. Shukla, A. Nogga and D. R. Phillips, *Nucl. Phys. A* **819**, 98 (2009) [[arXiv:0812.0138](#) [nucl-th]].

- [28] A. Margaryan, B. Strandberg, H. W. Griesshammer, J. A. McGovern, D. R. Phillips and D. Shukla, *Eur. Phys. J. A* **54**, no. 7, 125 (2018) [[arXiv:1804.00956](#) [nucl-th]].
- [29] L. S. Myers *et al.*, *Phys. Rev. C* **90**, no. 2, 027603 (2014) [[arXiv:1405.5049](#) [nucl-ex]].
- [30] M. H. Sikora *et al.*, *Phys. Rev. C* **96**, no. 5, 055209 (2017).
- [31] X. Li *et al.*, *Phys. Rev. C* **101**, no. 3, 034618 (2020) [[arXiv:1912.06915](#) [nucl-ex]].
- [32] L. S. Myers *et al.* [COMPTON@MAX-lab Collaboration], *Phys. Rev. Lett.* **113** (2014) 262506 [[arXiv:1409.3705](#) [nucl-ex]].
- [33] L. S. Myers *et al.*, *Phys. Rev. C* **92** (2015) 025203 [[arXiv:1503.08094](#) [nucl-ex]].
- [34] L. Myers *et al.*, *Phys. Rev. C* **89**, no.3, 035202 (2014).
- [35] M. W. Ahmed and C. R. Howell, private communication (2020).
- [36] P. P. Martel and E. J. Downie, private communication (2020).
- [37] C. R. Howell *et al.*: *A Next Generation Laser-Compton Gamma-Ray Source*, White Paper commissioned by the US Department of Energy, Office of Science, Nuclear Physics, forthcoming.
- [38] S. R. Beane, M. Malheiro, D. R. Phillips and U. van Kolck, *Nucl. Phys. A* **656**, 367 (1999) [[nucl-th/9905023](#)].
- [39] S. Pastore, J. Carlson, S. Gandolfi, R. Schiavilla and R. B. Wiringa, *Phys. Rev. C* **101**, no.4, 044612 (2020) [[arXiv:1909.06400](#) [nucl-th]].
- [40] V. Pascalutsa and D. R. Phillips, *Phys. Rev. C* **67**, 055202 (2003) [[arXiv:nucl-th/0212024](#) [nucl-th]].
- [41] S. Weinberg, *Phys. Lett. B* **251**, 288 (1990).
- [42] U. van Kolck, *PhD thesis*, University of Texas at Austin (1993).
- [43] U. van Kolck, *Phys. Rev. C* **49**, 2932 (1994).
- [44] J. L. Friar, *Few Body Syst.* **22**, 161 (1997) [[nucl-th/9607020](#)].
- [45] A. R. Edmonds, “Angular Momentum in Quantum Mechanics”, Princeton University Press (1974).
- [46] M. Tanabashi *et al.* [Particle Data Group], *Phys. Rev. D* **98**, no. 3, 030001 (2018) <http://pdg.lbl.gov>.
- [47] R. P. Hildebrandt, H. W. Griesshammer and T. R. Hemmert, *Eur. Phys. J. A* **46**, 111 (2010) [[nucl-th/0512063](#)].

- [48] S. R. Beane, M. Malheiro, J. A. McGovern, D. R. Phillips and U. van Kolck, Phys. Lett. B **567**, 200 (2003) Erratum: [Phys. Lett. B **607**, 320 (2005)] [[nucl-th/0209002](#)].
- [49] H. W. Griesshammer, Eur. Phys. J. A **49** (2013) 100; Errata: Eur. Phys. J. A **53** (2017) 113 and Eur. Phys. J. A **54** (2018) 57 [[arXiv:1304.6594](#) [nucl-th]].
- [50] A. Nogga, D. Huber, H. Kamada and W. Gloeckle, Phys. Lett. B **409**, 19 (1997) [[nucl-th/9704001](#)].
- [51] E. Epelbaum, A. Nogga, W. Gloeckle, H. Kamada, U. G. Meißner and H. Witala, Phys. Rev. C **66**, 064001 (2002) [[nucl-th/0208023](#)].
- [52] J. W. Chen, H. W. Griesshammer, M. J. Savage and R. P. Springer, Nucl. Phys. A **644**, 245 (1998) [[nucl-th/9809023](#)].
- [53] J. Kirscher, M. Birse, J. A. McGovern, H. W. Griesshammer and N. Walet, in preparation.
- [54] L. Andreoli, V. Cirigliano, S. Gandolfi and F. Pederiva, Phys. Rev. C **99**, no. 2, 025501 (2019) [[arXiv:1811.01843](#) [nucl-th]].
- [55] P. Maris *et al.*, EPJ Web Conf. **113**, 04015 (2016).
- [56] V. V. Kotlyar, H. Kamada, W. Gloeckle and J. Golak, Few Body Syst. **28**, 35 (2000) [[nucl-th/9903079](#)].
- [57] J. J. Sakurai, “Modern Quantum Mechanics”, Addison-Wesley (1994).